



**HAL**  
open science

## A physically-based model for retrieving foliar biochemistry and leaf orientation using close-range imaging spectroscopy

S. Jay, R. Bendoula, X. Hadoux, Jean-Baptiste Féret, N. Gorretta

► **To cite this version:**

S. Jay, R. Bendoula, X. Hadoux, Jean-Baptiste Féret, N. Gorretta. A physically-based model for retrieving foliar biochemistry and leaf orientation using close-range imaging spectroscopy. *Remote Sensing of Environment*, 2016, 177, pp.220-236. 10.1016/j.rse.2016.02.029 . hal-01804958

**HAL Id: hal-01804958**

**<https://hal.science/hal-01804958v1>**

Submitted on 1 Jun 2018

**HAL** is a multi-disciplinary open access archive for the deposit and dissemination of scientific research documents, whether they are published or not. The documents may come from teaching and research institutions in France or abroad, or from public or private research centers.

L'archive ouverte pluridisciplinaire **HAL**, est destinée au dépôt et à la diffusion de documents scientifiques de niveau recherche, publiés ou non, émanant des établissements d'enseignement et de recherche français ou étrangers, des laboratoires publics ou privés.

# A physically-based model for retrieving foliar biochemistry and leaf orientation using close-range imaging spectroscopy

Sylvain Jay<sup>a,\*</sup>, Ryad Bendoula<sup>a</sup>, Xavier Hadoux<sup>b,c</sup>, Jean-Baptiste Féret<sup>d</sup>,  
Nathalie Gorretta<sup>a</sup>

<sup>a</sup>*Irstea, UMR ITAP, 361 rue J.F. Breton, 34196 Montpellier, France*

<sup>b</sup>*Centre for Eye Research Australia, Royal Victorian Eye and Ear Hospital, Melbourne,  
Australia*

<sup>c</sup>*Ophthalmology, University of Melbourne, Department of Surgery, Melbourne, Australia*

<sup>d</sup>*Irstea, UMR TETIS, Maison de la Télédétection, 500 rue J.F. Breton, 34093  
Montpellier, France*

---

## Abstract

Radiative transfer models have long been used to characterize the foliar content at the leaf and canopy levels. However, they still do not apply well to close-range imaging spectroscopy, especially because directional effects are usually not taken into account. For this purpose, we introduce a physical approach to describe and simulate the variation in leaf reflectance observed at this scale. Two parameters are thus introduced to represent (1) specular reflection at the leaf surface and (2) local leaf orientation. The model, called COSINE (CLOse-range Spectral ImagiNg of lEaves), can be coupled with a directional-hemispherical reflectance model of leaf optical properties to relate

---

\*Corresponding author at: Irstea, UMR ITAP, 361 rue J.F. Breton, 34196 Montpellier, France. Tel: +33467166459.

*E-mail addresses:* sylvain.jay@irstea.fr (S. Jay), ryad.bendoula@irstea.fr (R. Bendoula), xavier@hadoux.com (X. Hadoux), jean-baptiste.feret@teledetection.fr (J.B. Féret), nathalie.gorretta@irstea.fr (N. Gorretta).

the measured reflectance to the foliar content. In this study, we show that, when combining COSINE with the PROSPECT model, the overall PROCOSINE model allows for a robust sub-millimeter retrieval of foliar content based on numerical inversion and pseudo bidirectional reflectance factor hyperspectral measurements.

The relevance of the added parameters is first shown through a sensitivity analysis performed in the visible and near-infrared (VNIR) and shortwave infrared (SWIR) ranges. PROCOSINE is then validated based on VNIR and SWIR hyperspectral images of various leaf species exhibiting different surface properties. Introducing these two parameters within the inversion allows us to obtain accurate maps of PROSPECT parameters, e.g., the chlorophyll content in the VNIR range, and the equivalent water thickness and leaf mass per area in the SWIR range. Through the estimation of light incident angle, the PROCOSINE inversion also provides information on leaf orientation, which is a critical parameter in vegetation remote sensing.

*Keywords:* close-range, COSINE, hyperspectral, imaging spectroscopy, leaf optical properties, pigment retrieval, PROCOSINE, PROSPECT, radiative transfer, vegetation

---

## 1. Introduction

2 Due to the strong interactions occurring between vegetation and the in-  
3 coming optical radiation through absorption and scattering processes, hyper-  
4 spectral remote sensing from satellites and aircrafts provides critical infor-  
5 mation to assess the spatial and temporal variabilities of vegetation status  
6 from local to global scales. This has led to a number of agricultural, envi-

7 ronmental and ecological applications such as the retrieval of leaf pigments  
8 (Zarco-Tejada et al., 2004; Ustin et al., 2009), the early detection of leaf  
9 diseases (Mahlein et al., 2013) or the mapping of forest biodiversity (Féret  
10 & Asner, 2014). As hyperspectral cameras are now becoming more afford-  
11 able, close-range remote sensing data are also increasingly available to the  
12 scientific community. Compared with air- and satellite-borne data, they gen-  
13 erally offer a sub-milliter or millimeter spatial resolution, and they can be  
14 acquired at a higher temporal frequency, which is particularly interesting for  
15 precision agriculture. For example, these data can be used to identify plant  
16 pigments (Blackburn, 2007), freezing stress (Nicotra et al., 2003) or leaf dis-  
17 eases (Mahlein et al., 2013), each of which is of tremendous importance to  
18 follow up the plant physiological status. These images are generally processed  
19 by applying statistically-based methods to estimate various leaf biochemical  
20 properties (Nicotra et al., 2003; Vigneau et al., 2011; Ji-Yong et al., 2012; Jay  
21 et al., 2014). However, at this scale, a proper physical interpretation based  
22 on radiative transfer modeling is needed to describe the interactions between  
23 light and vegetation, especially for a spatially- and temporally-resolved quan-  
24 tification of pigments (Blackburn, 2007).

25

26 Vegetation radiative transfer models are physically-based and simulate  
27 light propagation within leaves and/or canopies, e.g., as a function of leaf  
28 biochemical constituents, leaf anatomy or canopy structure. Whenever pos-  
29 sible, model inversion allows for the retrieval of the variables of interest,  
30 generally using iterative optimization, look-up tables, statistical methods or  
31 machine learning algorithms.

32 At the leaf level, these models range from simple plate models, to ray-tracing,  
33 radiosity and stochastic models that are computationally more difficult to in-  
34 vert (Dorigo et al., 2007). For instance, PROSPECT (Jacquemoud & Baret,  
35 1990) is based on the generalized plate model, and is particularly well suited  
36 to estimate leaf biochemical constituents (e.g., chlorophyll content, water  
37 content and leaf mass per area) based on spectral measurements in the op-  
38 tical domain. The main reasons for the popularity of PROSPECT are its  
39 accuracy, its computational efficiency (resulting in fast iterative model inver-  
40 sion) and free distribution.

41 At the canopy level, various approaches of different complexities have been  
42 developed for radiative transfer modeling, e.g., turbid medium approaches  
43 (Verhoef, 1984), geometrical approaches (Chen & Leblanc, 1997) or the com-  
44 bination of both (Gastellu-Etchegorry et al., 1996). Most of these models al-  
45 low the canopy reflectance to be modeled as a function of parameters related  
46 to canopy structure (such as leaf area index or leaf inclination distribution  
47 function), leaf optical properties and sun-sensor geometry.

48

49 However, leaf and canopy radiative transfer models do not apply well  
50 to close-range imaging spectroscopy. For example, at the leaf level, the  
51 directional-hemispherical reflectance and transmittance simulated by PROSPECT  
52 (Jacquemoud & Baret, 1990) are usually measured with an integrating sphere,  
53 whose implementation is difficult (if not impossible) for every single pixel of  
54 hyperspectral images. As a result, PROSPECT cannot be inverted based on  
55 directional reflectance data as retrieved by a close-range hyperspectral cam-  
56 era, unless it is assumed that leaves are Lambertian (Buddenbaum & Hill,

57 2015) and in fully horizontal position, which is an unrealistic hypothesis.  
58 Indeed, in most cases, leaf reflectance exhibits some anisotropy (Bousquet  
59 et al., 2005; Comar et al., 2012) and thus varies with respect to illumination  
60 and viewing angles. Furthermore, variation in leaf orientation prevent from  
61 achieving a proper reflectance correction for every pixel, because the refer-  
62 ence surface used for reflectance correction is generally not submitted to the  
63 same local illumination conditions than leaf material.

64 At the canopy level, most radiative transfer models have to be applied to  
65 mixed pixels (containing both soil and leaf materials), for which effects of  
66 leaf composition, canopy structure, soil properties and viewing/illumination  
67 angles are integrated into a single spectrum. Canopy models are thus well  
68 suited for ground-based spectroradiometric measurements, as well as for air-  
69 and satellite-borne hyperspectral measurements, all of them being usually  
70 characterized by a spatial resolution coarser than one meter (Zarco-Tejada  
71 et al., 2003; Colombo et al., 2008; Schlemmer et al., 2013). However, most  
72 canopy models are not suitable for simulating hyperspectral data character-  
73 ized by a higher spatial resolution (up to sub-millimeter level) for which the  
74 assumption of mixed pixel does not hold.

75

76 In this study, we propose a physically-based model, called COSINE (ClOse-  
77 range Spectral ImagiNg of lEaves), that describes the additional spectral  
78 variability induced by directional effects and variation in leaf orientation.  
79 Combining COSINE with a leaf directional-hemispherical reflectance model  
80 such as PROSPECT allows the simulation of leaf reflectance according to  
81 our experimental conditions: submillimetric spatial resolution and a single

82 light source assumed to be directional. When applied in inverse mode to  
83 close-range hyperspectral images, the overall PROCOSINE model enables  
84 the simultaneous retrieval of PROSPECT parameters (e.g., chlorophyll and  
85 water contents), bidirectional effects and leaf angle with respect to the light  
86 source.

87

88 The COSINE theory is described in Section 2. After recalling the nec-  
89 essary radiometric definitions, we develop a physically-based analytic ex-  
90 pression of the reflectance quantity retrieved using close-range imaging spec-  
91 troscopy. This expression is then related to PROSPECT to explain variations  
92 in leaf biochemistry and leaf anatomy. In Section 3, we present the data sets  
93 used in this article as well as details about model validation and sensitivity  
94 analysis. Results are presented and discussed in Section 4, and we finally  
95 draw some conclusions and perspectives in Section 5.

## 96 **2. Theory**

### 97 *2.1. Radiometric considerations*

#### 98 *2.1.1. Definitions*

99 The definitions and notations of the main physical quantities used in this  
100 article and summarized in Table 1, are based on the initial terminology of  
101 Nicodemus et al. (1977), which has later been reviewed by Schaepman-Strub  
102 et al. (2006).

103 The spectral radiance  $L$  is the radiant flux in a beam per unit wavelength,  
104 per unit area and per unit solid angle, and is expressed in the SI unit  
105  $[\text{W}\cdot\text{sr}^{-1}\cdot\text{m}^{-2}\cdot\text{nm}^{-1}]$ . This is the physical quantity measured by a hyper-

Table 1: Main parameters and acronyms.

Parameter	Definition [unit]
$b_{spec}$	Specular term [unitless]
$C_{ab}$	Chlorophyll a+b content [ $\mu\text{g.cm}^{-2}$ ]
$C_{bp}$	Brown pigment content [unitless]
$C_{cx}$	Carotenoid content [ $\mu\text{g.cm}^{-2}$ ]
$C_m$	Leaf mass per area [ $\text{g.cm}^{-2}$ ]
$C_w$	Equivalent water thickness [cm]
$E$	Spectral irradiance [ $\text{W.m}^{-2}.\text{nm}^{-1}$ ]
$f_r$	Bidirectional reflectance distribution function (BRDF) [ $\text{sr}^{-1}$ ]
$L$	Spectral radiance [ $\text{W.sr}^{-1}.\text{m}^{-2}.\text{nm}^{-1}$ ]
$\lambda$	Wavelength [nm]
$N$	Leaf structure parameter [unitless]
$\varphi_l$	Difference between illumination and leaf normal azimuth angles [ $^\circ$ ]
$\varphi_v$	Difference between illumination and viewing azimuth angles [ $^\circ$ ]
$R$	Bidirectional reflectance factor (BRF) [unitless]
$R_{hsi}$	Pseudo bidirectional reflectance factor [unitless]
$\rho$	Directional-hemispherical reflectance (DHR) [unitless]
$\theta_i$	Light incident angle (angle between the light source and the normal to the leaf) [ $^\circ$ ]
$\theta_l, \theta_v, \theta_s$	Leaf normal, viewing and illumination zenith angles [ $^\circ$ ]
$\vartheta$	PROCOSINE parameters
$\vartheta_{dhr}$	Parameters of the leaf DHR model



106 spectral imaging sensor after spectral calibration. The spectral irradiance  $E$   
107 is the radiant flux in a beam per unit wavelength and per unit area and is  
108 expressed in  $[\text{W}\cdot\text{m}^{-2}\cdot\text{nm}^{-1}]$ .

109 One of the main physical quantities used to describe angular patterns of  
110 reflected light is the bidirectional reflectance distribution function (BRDF)  
111 expressed in  $[\text{sr}^{-1}]$ . It describes how a parallel beam of incident light from  
112 one direction in the hemisphere is reflected into another direction in the  
113 hemisphere:

$$f_r(\theta_s; \theta_v, \varphi_v; \lambda) = \frac{dL_r(\theta_s; \theta_v, \varphi_v; \lambda)}{dE_i(\theta_s; \lambda)} \quad (1)$$

114 where subscripts  $i$  and  $r$  refer to incoming and reflected lights respectively,  
115  $\theta_s$  and  $\theta_v$  are respectively the illumination and viewing zenith angles, and  
116  $\varphi_v$  is the viewing azimuth angle relatively to the illumination azimuth an-  
117 gle (see Fig. 1 for angle representation). The BRDF being the ratio of two  
118 infinitesimal quantities, it cannot theoretically be measured. However, its  
119 integration over the corresponding solid angles allows the derivation of many  
120 other measurable physical quantities.

121 Usually, the reflectance correction process does not consist in retrieving di-  
122 rectly the reflectance (defined as the ratio of the leaving radiant exitance  
123 to the incident irradiance), but rather follows the definition of a reflectance  
124 factor. In the specific case of single illumination and viewing directions, the  
125 bidirectional reflectance factor (BRF, denoted by  $R$ ) is given by the ratio of  
126 the radiant flux  $dL_r$  reflected from the area element  $dA$  to the radiant flux  
127  $dL_r^{id}$  reflected from an ideal and diffuse surface of the same area  $dA$  under  
128 identical illumination and viewing geometries. It is unitless and, as developed

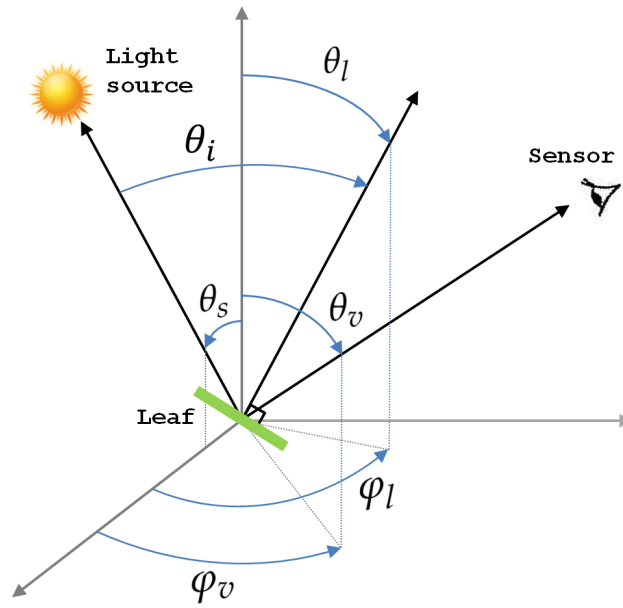


Figure 1: Angle representation.

129 by Schaepman-Strub et al. (2006), it can be expressed as follows:

$$R(\theta_s; \theta_v, \varphi_v; \lambda) = \frac{dL_r(\theta_s; \theta_v, \varphi_v; \lambda)}{dL_r^{id}(\theta_s; \lambda)} \quad (2)$$

130 where  $dL_r^{id}$  does not depend on viewing angles because of the Lambertian  
 131 nature of the reference surface.

132 The BRDF of an ideal and diffuse surface being  $(1/\pi)$ , the BRDF of any surface  
 133 is therefore related to its BRDF by:

$$R(\theta_s; \theta_v, \varphi_v; \lambda) = \pi f_r(\theta_s; \theta_v, \varphi_v; \lambda). \quad (3)$$

134 Let us finally define the directional-hemispherical reflectance (DHR) as the  
 135 integration of BRDF over the whole viewing hemisphere. The DHR is unitless  
 136 and is given by:

$$\rho(\theta_s; 2\pi; \lambda) = \int_0^{2\pi} \int_0^{\pi/2} f_r(\theta_s; \theta_v, \varphi_v; \lambda) \cos \theta_v \sin \theta_v d\theta_v d\varphi_v. \quad (4)$$

137 In the following, the spectral dependence will be omitted for more clarity in  
138 notation. Similarly, spectral radiance and spectral irradiance will be simply  
139 referred to as radiance and irradiance.

#### 140 *2.1.2. Radiometric expression of close-range hyperspectral measurement*

141 The solid angles corresponding to incident and reflected light beams are  
142 never purely directional, so rigorously, sensor measurements only allow the  
143 retrieval of a biconical reflectance factor (Schaepman-Strub et al., 2006).  
144 However, a close approximation of bidirectional reflectance can be obtained  
145 under specific experimental and instrumental conditions, e.g., using a col-  
146 limated light beam and a small sensor field of view (FOV) provided by a  
147 push-broom hyperspectral camera. In this case, the leaf BRF  $R$  is approxi-  
148 mated as follows:

$$R(\theta_s; \theta_v, \varphi_v) \approx \frac{L_r(\theta_s; \theta_v, \varphi_v)}{L_r^{id}(\theta_s)} \quad (5)$$

149 where  $L_r$  and  $L_r^{id}$  are the radiances respectively measured on the leaf and on  
150 the reference surface with a hyperspectral camera.

151 Importantly, Eq. 5 requires the leaf and reference surface to be under identi-  
152 cal illumination geometry (i.e., same  $\theta_s$  values). However, at the pixel level,  
153 the leaf position and leaf local orientation can make the irradiances received  
154 by the leaf and reference surface strongly different. Indeed, considering a  
155 directional light source, the irradiance received by an area element is propor-  
156 tional to the cosine of the incident angle  $\theta_i$ , i.e., the angle between the light  
157 source and the normal to this element:

$$E_i(\theta_i) = E_0 \cos \theta_i \quad (6)$$

158 where  $E_0$  is the irradiance received by an area element perpendicular to the  
 159 light source direction, and  $\cos \theta_i = \cos \theta_s \cos \theta_l + \sin \theta_s \sin \theta_l \cos \varphi_l$  where  $\theta_l$   
 160 and  $\varphi_l$  characterize the normal to this area element (Bousquet et al., 2005;  
 161 Comar et al., 2014).

162 Therefore, we define two illumination geometries corresponding to either the  
 163 leaf or the reference surface. The irradiance received by the leaf is:

$$E_i^l(\theta_i^l) = E_0 \cos \theta_i^l \quad (7)$$

164 whereas the one received by the ideal and diffuse reference surface is:

$$E_i^{id}(\theta_i^{id}) = E_0 \cos \theta_i^{id}. \quad (8)$$

165 The reference surface is usually positioned horizontally so, in the following,  
 166 we note  $\theta_i^{id} = \theta_s$  and  $\theta_i^l = \theta_i$ .

167 Similarly to Eq. 5, at each pixel, the physical quantity  $R_{hsi}$  retrieved using  
 168 a hyperspectral camera is given by:

$$R_{hsi}(\theta_s, \theta_i; \theta_v, \varphi_v) \approx \frac{L_r(\theta_i; \theta_v, \varphi_v)}{L_r^{id}(\theta_s)}. \quad (9)$$

169 Assuming the light source is directional and the pixel FOV is small, combin-  
 170 ing Eq. 1 and Eq. 9 leads to the following equation:

$$R_{hsi}(\theta_s, \theta_i; \theta_v, \varphi_v) \approx \frac{f_r(\theta_i; \theta_v, \varphi_v) E_i^l(\theta_i)}{(1/\pi) E_i^{id}(\theta_s)}. \quad (10)$$

171 Using Eq. 3, Eq. 7 and Eq. 8,  $R_{hsi}$  can finally be expressed as follows:

$$R_{hsi}(\theta_s, \theta_i; \theta_v, \varphi_v) \approx R(\theta_i; \theta_v, \varphi_v) \frac{\cos \theta_i}{\cos \theta_s}. \quad (11)$$

172 Eq. 11 reveals that the physical reflectance quantity retrieved from a small  
 173 FOV sensor in presence of a directional light source does not correspond

174 to the leaf BRDF if the leaf and reference surface are differently tilted with  
175 respect to the light source. In the following, we call "leaf pseudo BRDF" the  
176 leaf BRDF weighted by the ratio of the cosine of the angle between the light  
177 source and the normal to the leaf, to the cosine of illumination zenith angle.  
178 Therefore, Eq. 11 relates the measured leaf pseudo BRDF to the illumination  
179 zenith angle, the incident angle (related to local leaf angles and illumination  
180 zenith angle) and the leaf BRDF. To relate the latter to the foliar content, it  
181 is then necessary to take into account leaf surface properties as described in  
182 the next section.

## 183 *2.2. COSINE: a model for Close-range Spectral Imaging of Leaves*

184 In this study, we propose to adapt a leaf DHR model (such as PROSPECT  
185 (Jacquemoud & Baret, 1990) or LIBERTY (Dawson et al., 1998)) to the close-  
186 range case. Indeed, with the perspective of comparing leaf optical measure-  
187 ments to DHR simulations, proper experimental acquisitions require using an  
188 integrating sphere in order to match with the hemispherical simulations. As  
189 a result, leaf DHR models cannot directly be applied to hyperspectral remote  
190 sensing observations of vegetation that are affected by variable bidirectional  
191 effects (or BRDF effects) depending on illumination and viewing geometries.  
192 An important prerequisite before using these models for close-range imaging  
193 spectroscopy, is therefore to relate the leaf DHR to the leaf BRDF.

### 194 *2.2.1. Relationship between leaf BRDF and DHR*

195 It is generally admitted that the leaf BRDF is the sum of a diffuse compo-  
196 nent  $f_{r,diff}$  and a directional component  $f_{r,spec}$  (Bousquet et al., 2005; Comar

197 et al., 2014):

$$f_r(\theta_i; \theta_v, \varphi_v) = f_{r,spec}(\theta_i; \theta_v, \varphi_v) + f_{r,diff}(\theta_i; \theta_v, \varphi_v). \quad (12)$$

198 The diffuse component  $f_{r,diff}$  characterizes absorption and scattering pro-  
199 cesses within the leaf volume and thus depends on optically-active biochemi-  
200 cal and biophysical parameters. The directional component  $f_{r,spec}$  character-  
201 izes leaf surface properties and describes how light is reflected at the surface.  
202 While  $f_{r,diff}$  is strongly wavelength-dependent,  $f_{r,spec}$  is assumed to be nearly  
203 wavelength-independent in the visible and near-infrared (VNIR) range (be-  
204 tween 400 and 1000 nm) (Bousquet et al., 2005; Comar et al., 2014). In  
205 the shortwave infrared (SWIR) range (between 1000 and 2500 nm), this as-  
206 sumption does not hold because the leaf refractive index actually depends on  
207 wavelength (Féret et al., 2008; Vanderbilt & Grant, 1985), especially due to  
208 the non-negligible influence of water absorption.

209

210 As a first approximation,  $f_{r,diff}$  can be expressed as the ratio of leaf  
211 mesophyll Lambert coefficient  $k_l$  to  $\pi$  (Bousquet et al., 2005). To take into  
212 account the two-layer leaf structure (i.e. composed of an upper wax layer and  
213 a bottom leaf mesophyll layer), one should also consider the fraction of light  
214 that is reflected by the first wax layer and that does not reach the bottom  
215 layer (Stuckens et al., 2009; Ashikmin et al., 2000). The diffuse component  
216 is then expressed as a function of leaf mesophyll Lambert coefficient  $k_l$  and  
217 wax DHR  $\rho_{spec}$  (Stuckens et al., 2009):

$$f_{r,diff}(\theta_i) = \frac{k_l}{\pi}(1 - \rho_{spec}(\theta_i; 2\pi)) \quad (13)$$

where  $f_{r,diff}$  does not depend on viewing angles and  $k_l$  only depends on

wavelength.

As defined by Eq. 4, the total DHR can then be obtained combining Eq. 12 and Eq. 13:

$$\begin{aligned} \rho(\theta_i; 2\pi) = & \int_0^{2\pi} \int_0^{\pi/2} f_{r,spec}(\theta_i; \theta_v, \varphi_v) \cos \theta_v \sin \theta_v d\theta_v d\varphi_v \\ & + \frac{k_l}{\pi} (1 - \rho_{spec}(\theta_i; 2\pi)) \int_0^{2\pi} \int_0^{\pi/2} \cos \theta_v \sin \theta_v d\theta_v d\varphi_v \end{aligned} \quad (14)$$

218 which can be rewritten as follows:

$$\rho(\theta_i; 2\pi) = \rho_{spec}(\theta_i; 2\pi) + k_l(1 - \rho_{spec}(\theta_i; 2\pi)). \quad (15)$$

219 This equation provides the necessary basis to relate a leaf DHR model to the  
 220 leaf BRDF (through the Lambert coefficient).

### 221 2.2.2. The COSINE model

222 Assuming nadir illumination, a leaf DHR model expresses the DHR  $\rho(0; 2\pi)$   
 223 as a function of leaf biochemical and biophysical contents characterized by  
 224 the vector of input parameters  $\boldsymbol{\vartheta}_{dhr}$ . Following Eq. 15, the modeled Lam-  
 225 bert coefficient can be expressed as a function of  $\rho_{spec}(0; 2\pi)$  and DHR model  
 226  $\tilde{\rho}(\boldsymbol{\vartheta}_{dhr})$  as:

$$\tilde{k}_l(\boldsymbol{\vartheta}_{dhr}) = \frac{\tilde{\rho}(\boldsymbol{\vartheta}_{dhr}) - \rho_{spec}(0; 2\pi)}{1 - \rho_{spec}(0; 2\pi)} \quad (16)$$

where  $\sim$  refers to modeled quantities.

The leaf BRDF can then be modeled as a function of leaf parameters  $\boldsymbol{\vartheta}_{dhr}$  by combining Eq. 12, Eq. 13 and Eq. 16:

$$\begin{aligned} \tilde{f}_r(\theta_i; \theta_v, \varphi_v; \boldsymbol{\vartheta}_{dhr}) = & f_{r,spec}(\theta_i; \theta_v, \varphi_v) \\ & + \frac{1}{\pi} \left( \frac{1 - \rho_{spec}(\theta_i; 2\pi)}{1 - \rho_{spec}(0; 2\pi)} \right) (\tilde{\rho}(\boldsymbol{\vartheta}_{dhr}) - \rho_{spec}(0; 2\pi)). \end{aligned} \quad (17)$$

In order to estimate  $\boldsymbol{\vartheta}_{dhr}$  from the pseudo BRF  $R_{hsi}$  retrieved using a hyperspectral camera, Eq. 3, Eq. 11 and Eq. 17 are combined to obtain the pseudo-BRF based COSINE model:

$$\begin{aligned} \widetilde{R}_{hsi}(\theta_s, \theta_i; \theta_v, \varphi_v; \boldsymbol{\vartheta}_{dhr}) = & \left( \frac{\cos \theta_i}{\cos \theta_s} \right) \left[ \left( \frac{1 - \rho_{spec}(\theta_i; 2\pi)}{1 - \rho_{spec}(0; 2\pi)} \right) \tilde{\rho}(\boldsymbol{\vartheta}_{dhr}) \right. \\ & \left. + \pi f_{r,spec}(\theta_i; \theta_v, \varphi_v) - \rho_{spec}(0; 2\pi) \left( \frac{1 - \rho_{spec}(\theta_i; 2\pi)}{1 - \rho_{spec}(0; 2\pi)} \right) \right] \quad (18) \end{aligned}$$

227 where only the first term of the sum is related to the leaf DHR model.  
228 Note that  $f_{r,spec}$  and  $\rho_{spec}$  could potentially be modeled using the leaf BRDF  
229 model developed by Bousquet et al. (2005) that expresses the directional  
230 component as a function of illumination and viewing geometries as well as on  
231 the wax refractive index and a surface roughness parameter. Unfortunately,  
232 the resulting model becomes over-parameterized so its inversion is an ill-posed  
233 problem and leads to poor estimation results (not shown).

### 234 2.2.3. A simplified COSINE model for the VNIR range

235 In the VNIR range, the second term in Eq. 18 is assumed to be wavelength-  
236 independent. Omitting its dependence in viewing angles, Eq. 18 can then be  
237 simplified as:

$$\widetilde{R}_{hsi}(\theta_s, \theta_i; \boldsymbol{\vartheta}_{dhr}, b_{spec}) = \left( \frac{\cos \theta_i}{\cos \theta_s} \right) \left[ \left( \frac{1 - \rho_{spec}(\theta_i; 2\pi)}{1 - \rho_{spec}(0; 2\pi)} \right) \tilde{\rho}(\boldsymbol{\vartheta}_{dhr}) + b_{spec} \right] \quad (19)$$

238 where  $b_{spec} = b_{spec}(\theta_i; \theta_v, \varphi_v) = \pi f_{r,spec}(\theta_i; \theta_v, \varphi_v) - \rho_{spec}(0; 2\pi) \left( \frac{1 - \rho_{spec}(\theta_i; 2\pi)}{1 - \rho_{spec}(0; 2\pi)} \right)$ .  
239 Assuming that the fraction  $\frac{1 - \rho_{spec}(\theta_i; 2\pi)}{1 - \rho_{spec}(0; 2\pi)}$  is nearly one (especially true for low  
240 incident angles), Eq. 19 can be approximated by:

$$\widetilde{R}_{hsi}(\theta_s, \theta_i; \boldsymbol{\vartheta}_{dhr}, b_{spec}) = \left( \frac{\cos \theta_i}{\cos \theta_s} \right) \left[ \tilde{\rho}(\boldsymbol{\vartheta}_{dhr}) + b_{spec} \right]. \quad (20)$$



241 COSINE therefore simulates the pseudo-BRF as a function of incident an-  
242 gle  $\theta_i$ , illumination zenith angle  $\theta_s$ , foliar content through the DHR model  
243 parameters  $\boldsymbol{\vartheta}_{dhr}$  and BRDF effect  $b_{spec}$ . Importantly, this model is presum-  
244 ably only well suited for low incident angles. In high incidence, the fraction  
245  $\frac{1-\rho_{spec}(\theta_i;2\pi)}{1-\rho_{spec}(0;2\pi)}$  may differ from one, which could lead to an incorrect estimation  
246 of  $\theta_i$  when inverting the model.  
247 Finally, in order to model directly radiance measurements, a radiance-based  
248 COSINE model can be derived from Eq. 9 as:

$$\widetilde{L}_r(\theta_s, \theta_i; \boldsymbol{\vartheta}_{dhr}, b_{spec}) = \left( \frac{\cos \theta_i}{\cos \theta_s} \right) \left[ \widetilde{\rho}(\boldsymbol{\vartheta}_{dhr}) + b_{spec} \right] L_r^{id}(\theta_s) \quad (21)$$

249 where  $L_r^{id}(\theta_s)$  is the radiance measured on the reference surface.

### 250 3. Material and methods

#### 251 3.1. Data acquisition

##### 252 3.1.1. Spectral measurements

253 The COSINE model was tested using close-range hyperspectral images  
254 acquired under laboratory conditions. Two push-broom hyperspectral cam-  
255 eras were used, i.e., a HySpex VNIR-1600 camera (Norsk Elektro Optikk,  
256 Norway) and a HySpex SWIR-320m-e camera (Norsk Elektro Optikk, Nor-  
257 way). The HySpex VNIR-1600 camera acquired successive lines of 1600 pixels  
258 and 160 spectral bands ranging from 415 to 994 nm with a 3.7 nm spectral  
259 sampling interval. The pixel FOV was 0.18 and 0.36 mrad across- and along-  
260 track respectively.

261 Even if COSINE is theoretically only well suited for the VNIR range for which  
262 the directional BRDF component is assumed to be wavelength-independent,

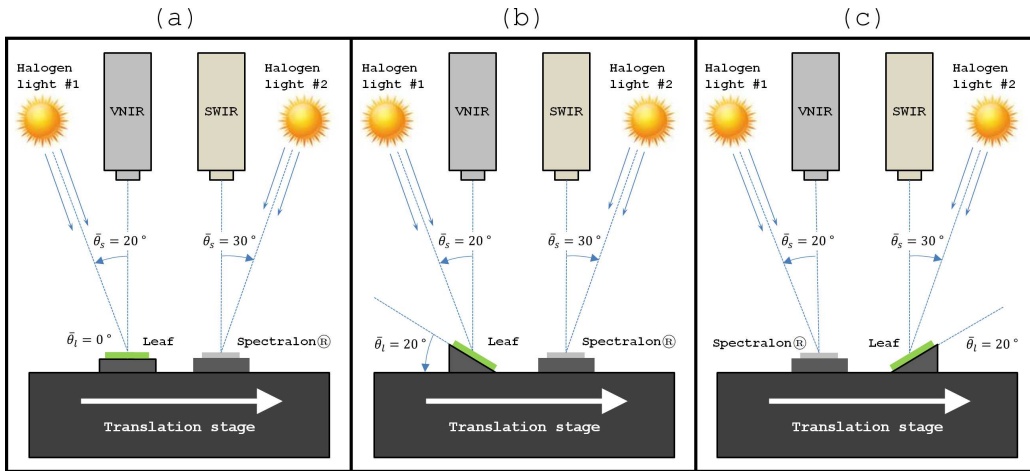


Figure 2: Experimental setup for the horizontal (a) and tilted (b-c) configurations. For the VNIR camera, the corresponding average incident angles  $\bar{\theta}_i$  are  $20^\circ$  (a),  $40^\circ$  (b) and  $0^\circ$  (c). For the SWIR camera, the corresponding average incident angles  $\bar{\theta}_i$  are  $30^\circ$  (a),  $10^\circ$  (b) and  $50^\circ$  (c).

263 we also tested this model on SWIR images in order to see how this assump-  
 264 tion was affecting the estimation results. The HySpex SWIR-320m-e camera  
 265 acquired successive lines of 320 pixels and 256 spectral bands ranging from  
 266 960 to 2490 nm with a 6 nm spectral sampling interval. The pixel FOV was  
 267 0.75 mrad across- and along-track.

268 As shown in Fig. 2, in both cases, the camera was facing towards nadir at  
 269 thirty centimeters above the imaged leaf, thus leading to across-track pixel  
 270 FOV of 0.23 mm for the SWIR camera, and 0.11 mm for the VNIR camera  
 271 (after an appropriate subsampling in the across-track direction so as to ob-  
 272 tain square pixels). Both cameras were positioned thirty centimeters apart.  
 273 The lighting was provided by two halogen sources (one for each camera)  
 274 positioned close to the cameras. These light sources were collimated and

275 positioned so that each source was illuminating the same line than the line  
276 imaged by the corresponding camera. The illumination zenith angles were  
277 set to  $\theta_s = 20^\circ$  and  $\theta_s = 30^\circ$  for the VNIR camera and the SWIR camera  
278 respectively. The incoming halogen irradiance was estimated on a line-by-  
279 line basis by using a reference surface (Spectralon<sup>®</sup>, Labsphere) horizontally  
280 placed next to the imaged leaf. In order to limit saturation on the reference  
281 surface while obtaining a low noise level in the strong absorption regions,  
282 we chose a Spectralon<sup>®</sup> whose diffuse reflectance was approximately 40%  
283 between 400 and 2500 nm. After acquisition, VNIR and SWIR images were  
284 finally calibrated to spectral radiance.

285

286 The main data set contains leaves from five species commonly found in  
287 the French Mediterranean region, namely bamboo (*Phyllostachys aurea*), ivy  
288 (*Hedera helix*), laurestine (*Viburnum tinus*), bay laurel (*Laurus nobilis*) and  
289 holly (*Ilex aquifolium*). Some of these leaves exhibited strong (resp. weak)  
290 non-Lambertian behavior, e.g., bay laurel and holly (resp. bamboo). Also,  
291 some of them had regular (resp. non-regular) surfaces, e.g., bay laurel (resp.  
292 ivy and holly). All of these leaves were harvested in March, 2015 and selected  
293 on a color basis, ranging from dark green for leaves with a high chlorophyll  
294 content, to yellow for senescent leaves. As illustrated in Fig. 2, each leaf was  
295 placed on a translation stage and was imaged in three positions using a  $20^\circ$   
296 tilted stand. As a result, the average incident angles  $\bar{\theta}_i$  were  $0^\circ$ ,  $20^\circ$  and  
297  $40^\circ$  for VNIR camera, and  $10^\circ$ ,  $30^\circ$  and  $50^\circ$  for SWIR camera. Note that  
298 the translation stage had low reflectivity so we assumed that, after being  
299 transmitted through the leaf, the light reflected from the translation stage

300 and re-transmitted through the leaf was negligible.

301 In addition, a SWIR image of a sugar beet leaf (*Beta vulgaris*) was ac-  
302 quired, especially because this species shows interesting features in this spec-  
303 tral range, i.e., very high equivalent water thickness ( $C_w > 0.02$  cm) and low  
304 leaf mass per area ( $C_m < 0.005$  g.cm<sup>-2</sup>), as well as a strongly non-Lambertian  
305 and non-regular surface, thereby illustrating well the relevance of our model.  
306 This leaf was only imaged in horizontal position, its surface being already  
307 highly non-regular.

### 308 3.1.2. Reference measurements

309 For each leaf, after spectral measurements, several leaf disks (from two to  
310 seven disks depending on leaf size) of known area were sampled using a cork  
311 borer. Each disk position was then recorded for further reference. A Dualex  
312 scientific+™ (Force-A, Orsay, France), hereafter called Dualex, was used to  
313 measure the chlorophyll a+b content  $C_{ab}$  in every disk. This leafclip allows  
314 non-destructive transmittance-based  $C_{ab}$  measurements characterized by an  
315 accuracy of around 5 μg.cm<sup>-2</sup> (Cerovic et al., 2012). Compared with the well  
316 known SPAD-502™ (Minolta, Japan), the Dualex uses a higher  $C_{ab}$ -sensitive  
317 wavelength (710 nm) that allows it to have a nearly linear response to vari-  
318 ation in  $C_{ab}$  for  $C_{ab} < 40$  μg.cm<sup>-2</sup>. However, for dicotyledons, saturation  
319 occurring beyond 40 μg.cm<sup>-2</sup> leads the Dualex to underestimate such  $C_{ab}$   
320 values (Cerovic et al., 2012). The higher  $C_{ab}$ , the greater the underestima-  
321 tion.

322 Leaf disks were then weighted and placed in a drying oven at 75°C for 48 h.  
323 Subsequently, their dry mass was measured to obtain the equivalent water

Table 2: Characteristics of reference measurements for the main data set.

Parameter	Number of samples	Mean	Min/Max	Standard deviation
$C_{ab}$ [ $\mu\text{g}\cdot\text{cm}^{-2}$ ]	93	29.4	5.2/54.6	11.1
$C_w$ [cm]	22	0.0104	0.0049/0.0164	0.0040
$C_m$ [ $\text{g}\cdot\text{cm}^{-2}$ ]	22	0.0091	0.0052/0.0129	0.0023

324 thickness  $C_w$  (in [cm]) and leaf mass per area  $C_m$  (in [ $\text{g}\cdot\text{cm}^{-2}$ ]) as follows:

$$C_w = \frac{FW - DW}{A} \times d_w \quad (22)$$

$$C_m = \frac{DW}{A} \quad (23)$$

325 where  $FW$  and  $DW$  are the fresh and dry weights of leaf disks respectively,  
326  $A$  is the total disk area, and  $d_w = 1 \text{ g}\cdot\text{cm}^{-3}$  is the water density.

327 Therefore, for each leaf, several measurements of  $C_{ab}$  and one measurement of  
328  $C_w$  and  $C_m$  were available. The ranges of  $C_{ab}$ ,  $C_w$  and  $C_m$  for the main data  
329 set are reported in Table 2 and were similar to those found in the literature  
330 (Féret et al., 2008; Danson & Bowyer, 2004).

### 331 3.2. Retrieval of leaf parameters from model inversion

332 In this study, we used the PROSPECT (Leaf Optical Properties Spectra)  
333 model to simulate the leaf DHR from 400 to 2500 nm as a function of the leaf  
334 biochemistry and structure. The original version developed by Jacquemoud  
335 & Baret (1990) has been successively improved over the years to take into  
336 account other biochemical components and a broader spectral range (Jacque-  
337 moud et al., 1996; Baret & Fourty, 1997a; Jacquemoud et al., 2000; Féret  
338 et al., 2008; Gerber et al., 2011). The considered PROSPECT 5b version was  
339 developed by Féret et al. (2008) (available at <http://teledetection.ipgp>).

340 [jussieu.fr/prosail/](http://jussieu.fr/prosail/)) and simulates the leaf DHR as a function of the leaf  
 341 structure parameter  $N$ , chlorophyll a+b content  $C_{ab}$ , carotenoid content  $C_{cx}$ ,  
 342 brown pigment content  $C_{bp}$ , equivalent water thickness  $C_w$  and leaf mass per  
 343 area  $C_m$ .

344 In the following, leaf parameters were retrieved based on model inversion.  
 345 The parameters that were only affecting the reflected radiation in the VNIR  
 346 range (resp. the SWIR range), were kept constant when considering the  
 347 SWIR range (resp. the VNIR range) so as to reduce the estimation un-  
 348 certainty. Therefore, because water absorption is weak in the VNIR range  
 349 and only occurs around 970 nm (Curran, 1989), the VNIR range was re-  
 350 duced to 410-900 nm (i.e., 135 bands) and  $C_w$  was fixed to the default value  
 351 0.01 cm. The vector of input PROSPECT parameters was thus  $\boldsymbol{\vartheta}_{dhr} =$   
 352  $[N, C_{ab}, C_{cx}, C_{bp}, C_m]^t$ . Similarly, foliar pigments do not affect the SWIR re-  
 353 flectance so  $C_{ab}$ ,  $C_{cx}$  and  $C_{bp}$  were fixed to the default values  $30 \mu\text{g}\cdot\text{cm}^{-2}$ ,  
 354  $10 \mu\text{g}\cdot\text{cm}^{-2}$  and 0 respectively. In the SWIR range, the vector of input  
 355 PROSPECT parameters was  $\boldsymbol{\vartheta}_{dhr} = [N, C_w, C_m]^t$ .

356 For each pixel, the combined pseudo-BRF based PROSPECT+COSINE model  
 357 (named PROCOSINE hereafter) was numerically inverted by optimizing the  
 358 following least square merit function:

$$\hat{\boldsymbol{\vartheta}}_{pseudo-brf} = \underset{\boldsymbol{\vartheta}}{\operatorname{argmin}} \sum_{\lambda_i} \left[ R_{hsi}(\lambda_i) - \widetilde{R}_{hsi}(\lambda_i; \boldsymbol{\vartheta}) \right]^2 \quad (24)$$

359 where  $\boldsymbol{\vartheta} = [\boldsymbol{\vartheta}_{dhr}, \theta_i, b_{spec}]^t$ ,  $R_{hsi}$  is the measured pseudo-BRF retrieved using  
 360 Eq. 9 and  $\widetilde{R}_{hsi}$  is the pseudo-BRF based PROCOSINE model given by Eq. 20.  
 361 Similarly, the radiance-based PROCOSINE model was inverted by solving

Table 3: Lower bounds, upper bounds and initial values of the optimization problem.

Parameter	Lower bound	Upper bound	Initial value
$N$	1	3.5	1.5
$C_{ab}$ [ $\mu\text{g}\cdot\text{cm}^{-2}$ ]	0	100	50
$C_{cx}$ [ $\mu\text{g}\cdot\text{cm}^{-2}$ ]	0	30	10
$C_{bp}$	0	5	0
$C_w$ [cm]	0.00005	0.1	0.01
$C_m$ [ $\text{g}\cdot\text{cm}^{-2}$ ]	0.001	0.03	0.01
$\theta_i$ [ $^\circ$ ]	0	90	20
$b_{spec}$	-0.2	0.6	0

362 the following optimization problem:

$$\hat{\boldsymbol{\vartheta}}_{radiance} = \underset{\boldsymbol{\vartheta}}{\operatorname{argmin}} \sum_{\lambda_i} \left[ L_r(\lambda_i) - \widetilde{L}_r(\lambda_i; \boldsymbol{\vartheta}) \right]^2 \quad (25)$$

363 where  $L_r$  is the measured spectral radiance and  $\widetilde{L}_r$  is the radiance-based  
364 PROCOSINE model given by Eq. 21.

365

366 To reduce the number of solutions to the inverse problem, the estimation  
367 range was restricted using lower and upper bounds. These bounds as well as  
368 initial values are provided in Table 3. Note that  $C_{bp}$  and  $C_w$  upper bounds  
369 are higher than those found in the literature because, at the sub-millimeter  
370 level,  $C_{bp}$  and  $C_w$  can be very high in necrotic regions and veins respectively.  
371 Optimization of Eq. 24 and Eq. 25 was performed using the trust-region  
372 reflective algorithm implemented in MATLAB<sup>®</sup> (version 8.0.0, The Math-  
373 Works Inc., Natick, MA, 2012) within the "lsqcurvefit" function.

374 *3.3. PROCOSINE sensitivity analysis*

375 Before assessing PROCOSINE in terms of estimation results, we per-  
376 formed a global sensitivity analysis in order to study the relative contribution  
377 of each parameter to the modeled pseudo-BRF as a function of wavelength.  
378 Global sensitivity analysis informs us on which variation in the model output  
379 is produced by variation in the model input parameters, both individually  
380 and collectively through their interactions with each other. When studied as  
381 a function of wavelength, it provides interesting insights regarding the opti-  
382 mal spectral bands that can be used to retrieve model parameters.

383

384 In this paper, we implemented the EFAST (Extended Fourier Amplitude  
385 Sensitivity Transform) method (Saltelli et al., 1999) that was already ap-  
386 plied to PROSAIL and PROGEOSAIL models by Bowyer & Danson (2004).  
387 EFAST is a quantitative variance-based method, i.e., it allows the deriva-  
388 tion of sensitivity indices from the decomposition of the total variance of the  
389 model output into variance terms induced by every input parameter. In this  
390 paper, we only used the first-order index  $S_i$  that represents the percentage  
391 of output variance explained by the  $i^{\text{th}}$  parameter alone. The remaining per-  
392 centage of variance is explained by interactions between parameters and is  
393 given by  $S_{int} = 1 - \sum_i S_i$ .  $S_i$  (and  $S_{int}$ ) ranges from 0 to 1, and the higher  
394  $S_i$ , the more sensitive the model output is to the  $i^{\text{th}}$  parameter.

395

396 In this study, 5000 combinations of model parameters were randomly gen-  
397 erated using appropriate probability distributions because the latter strongly  
398 affects the results of sensitivity analysis (Bowyer & Danson, 2004; Wallach



Table 4: Estimated parameter distributions ( $\mu$ : mean;  $\sigma$ : standard deviation;  $\alpha$ : shape parameter;  $\beta$ : scale parameter).

Parameter	Distribution	$\mu$	$\sigma$	$\alpha$	$\beta$
$N$	Gamma	1.52	0.23	47.50	0.032
$C_{ab}$ [ $\mu\text{g}\cdot\text{cm}^{-2}$ ]	Gamma	32.8	18.87	1.99	16.45
$C_{cx}$ [ $\mu\text{g}\cdot\text{cm}^{-2}$ ]	Gamma	8.51	3.92	3.83	2.22
$C_w$ [cm]	Gamma	0.0122	0.0061	6.45	0.0019
$C_m$ [ $\text{g}\cdot\text{cm}^{-2}$ ]	Gamma	0.0078	0.0036	4.20	0.0018
$\theta_i$ [ $^\circ$ ]	Gamma	25	10	6.25	4
$b_{spec}$ (VNIR)	Normal	-0.009	0.0375	-	-
$b_{spec}$ (SWIR)	Normal	0.0346	0.0403	-	-

399 et al., 2014). The distributions of PROSPECT parameters were estimated  
400 from seventeen independent data sets made available by Féret et al. (2011);  
401 Féret, personal communication. They include a wide range of leaf spec-  
402 tral, chemical, and structural properties, i.e., 1417 leaves corresponding to  
403 about 120 different species from various growing conditions and develop-  
404 mental stages. Note that  $C_{ab}$ ,  $C_{cx}$ ,  $C_w$  and  $C_m$  data were obtained in a  
405 destructive way, whereas  $N$  data were obtained from PROSPECT inversion  
406 on DHR data. It can be shown that these data are well described by Gamma  
407 distributions ( $p < 0.001$ ). Using such distributions (instead of normal ones)  
408 prevented us from generating samples with negative content values. Regard-  
409 ing brown pigments, we assumed that leaves under study were green so  $C_{bp}$   
410 was set to zero. Finally,  $\theta_i$  and  $b_{spec}$  distributions were retrieved from the  
411 estimation results presented in Section 4 using a Gamma distribution for  $\theta_i$   
412 and a normal distribution for  $b_{spec}$  (not shown). The characteristics of all of  
413 these distributions are presented in Table 4, where the shape parameter  $\alpha$

414 and the scale parameter  $\beta$  of the Gamma distribution were given by their  
415 maximum likelihood estimates. Note that two  $b_{spec}$  distributions were used  
416 for the two spectral domains. Importantly, the covariance between param-  
417 eters could not be considered when generating the samples. Consequently,  
418 the actual influences of  $C_{ab}$  and  $C_{cx}$  are likely to be slightly different, both  
419 parameters being highly correlated (Féret et al., 2008).  
420 For each EFAST run, 5000 leaf reflectance spectra were therefore simulated  
421 using PROSPECT and PROCOSINE (Eq. 20) so as to compute first-order  
422 indices and interactions. Average indices were finally computed over 15 runs.

## 423 4. Results and discussion

### 424 4.1. Sensitivity analysis

425 In Figure 3, we compare the first-order indices and interactions obtained  
426 with PROSPECT and PROCOSINE over the VNIR and SWIR ranges. Fig. 3.a  
427 and Fig. 3.b reveal the same features already observed in previous studies  
428 using other methods and/or models (Jacquemoud & Baret, 1990; Jacque-  
429 moud et al., 2009; Bacour et al., 2001, 2002; Bowyer & Danson, 2004). In  
430 the visible range (400-730 nm), photosynthetic pigments (i.e., chlorophyll  
431 and carotenoids) drive most of the reflectance variability. Between 400 and  
432 525 nm where the carotenoid absorption is the strongest (Féret et al., 2008),  
433 the contributions of  $C_{ab}$  and  $C_{cx}$  are similar in magnitude and range from  
434 20 to 40%. Between 525 and 730 nm, reflectance mainly depends on  $C_{ab}$ , its  
435 contribution ranging from 40 to 90%. The influence of interactions is higher  
436 in strong absorption regions, which means that the effects of other param-  
437 eters depend on  $C_{ab}$  and  $C_{cx}$  values. For example, the relative increase in

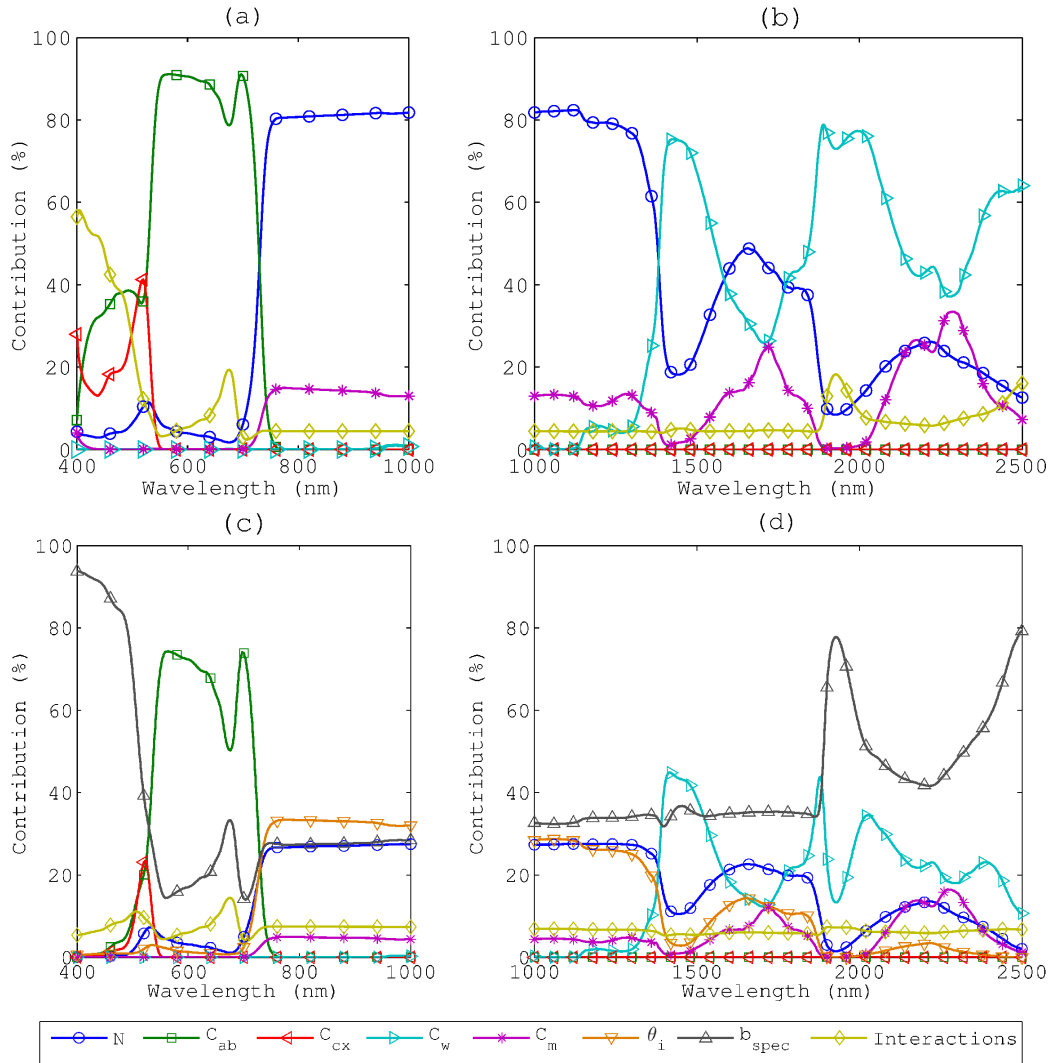


Figure 3: First-order sensitivity indices and interactions for (a) PROSPECT in the VNIR range, (b) PROSPECT in the SWIR range, (c) PROCOSINE in the VNIR range, and (d) PROCOSINE in the SWIR range ( $\theta_s = 26^\circ$ ).

438 reflectance due an increase in  $N$  (reflecting higher scattering within the leaf  
439 internal structure) will be high in case of low absorption and low in case of  
440 strong absorption.

441 In the NIR plateau, variation in reflectance is mainly produced by variation  
442 in leaf structure (80%) and leaf mass per area (14%) through scattering pro-  
443 cesses (Knyazikhin et al., 2013). In the SWIR range, only leaf structure,  
444 equivalent water thickness and leaf mass per area have significant contribu-  
445 tions. In particular,  $C_w$  strongly influences reflectance in the water absorp-  
446 tion peaks located around 1450 and 1950 nm (about 75%), whereas variation  
447 in  $C_m$  has a significant contribution around 1720 and 2250 nm (resp. 24%  
448 and 30%).

449

450 Taking into account BRDF effects and leaf orientation through the  $b_{spec}$   
451 and  $\theta_i$  parameters within the PROCOSINE model modifies the reflectance  
452 sensitivity as shown in Figure 3.c and Figure 3.d. Compared with PROSPECT  
453 sensitivity analysis, the overall contributions of PROSPECT parameters are  
454 mostly similar in shape but still, they decrease to account for variance in  
455  $b_{spec}$  and  $\theta_i$ . For example, the  $C_{ab}$  contribution at around 550 nm decreases  
456 from 90 to 70%.

457 The contributions of  $b_{spec}$  and  $\theta_i$  are quite different. Overall, variance in  
458  $b_{spec}$  highly influences reflectance in strong absorption regions (both due to  
459  $C_{ab}$  and  $C_w$ ), accounting for up to 90% near 400 nm and 75% near 1930  
460 and 2500 nm. In these regions, the diffuse part of reflectance is very low  
461 so the influence of the surface-reflected flux (that does not interact with the  
462 leaf volume) dominates. Interestingly, an analogy can be made with high-

463 resolution water remote sensing, in that the sun glint (i.e., the amount of  
464 flux directly reflected at the water surface) is usually estimated in the NIR  
465 region, where the water-leaving signal is negligible because of strong water  
466 absorption (Hochberg et al., 2003). Overall, the  $b_{spec}$  contribution is always  
467 greater than 15% between 400 and 2500 nm, thereby indicating that this pa-  
468 rameter should not be neglected when dealing with close-range hyperspectral  
469 images.

470

471 The contribution of the incident angle  $\theta_i$  significantly varies over the whole  
472 spectral domain. It mostly affects reflectance in the NIR plateau, accounting  
473 for about 30% of the variance of the PROCOSINE output. Conversely, its  
474 influence is much weaker in the visible range, where its contribution does  
475 not exceed 5%, as well as in water absorption regions. Generally, because  
476 it affects the model through a multiplicative term (see Eq. 20 and Eq. 21),  
477 the spectral profile of its contribution is similar to a common leaf spectral  
478 signature: the higher the reflectance, the higher its contribution. Interest-  
479 ingly, this profile is also similar to the contribution of the average leaf angle  
480 (ALA) to the PROSAIL model (Jacquemoud et al., 2009). In the latter case,  
481 ALA has more influence at weakly absorbing wavelengths because the effect  
482 of multiple scattering within the canopy is stronger (Knyazikhin et al., 2013).

483

484 To summarize, this sensitivity analysis shows that both  $b_{spec}$  and  $\theta_i$  sig-  
485 nificantly affect the measured signal and definitively have to be taken into  
486 account in the case of close-range imaging spectroscopy.

487 *4.2. Quantitative assessment of model inversion*

488 The performances of model inversion were quantitatively assessed both  
489 in terms of spectral fitting and parameter retrieval. Note that we had only  
490 reference measurements integrated over one (for  $C_{ab}$ ) or several (for  $C_w$  and  
491  $C_m$ ) leaf disk(s) of a few square centimeters. As a result, in this section,  
492 the means and standard deviations of  $C_{ab}$ ,  $C_w$  and  $C_m$  estimated values were  
493 computed from the values estimated within the corresponding leaf disk(s).

494 *4.2.1. PROCOSINE spectral accuracy*

495 We first quantified how accurate was PROCOSINE in fitting the pseudo-  
496 BRDF and radiance measurements retrieved at the pixel level. In Fig. 4, we  
497 show some fitting results obtained with an ivy leaf both for the VNIR and  
498 SWIR ranges, this leaf surface being non-Lambertian and non-regular.  
499 Overall, strong agreements were obtained between measured and simulated  
500 spectra in the two ranges (RMSE < 4%). As expected, high  $b_{spec}$  values were  
501 retrieved in areas affected by specular reflection, and high  $\theta_i$  values were  
502 retrieved where the light incident angle was high. Compared with the VNIR  
503 range, the obtained RMSE were about twice higher for the SWIR range.  
504 This is in agreement with the mismodeling of specular reflection in the SWIR  
505 range mentioned in Section 2.2.1 and discussed further in Section 4.2.4. These  
506 results thus demonstrate the accuracy of PROCOSINE in accounting for the  
507 spectral variability induced by BRDF effects and leaf orientation, especially  
508 in the VNIR range.

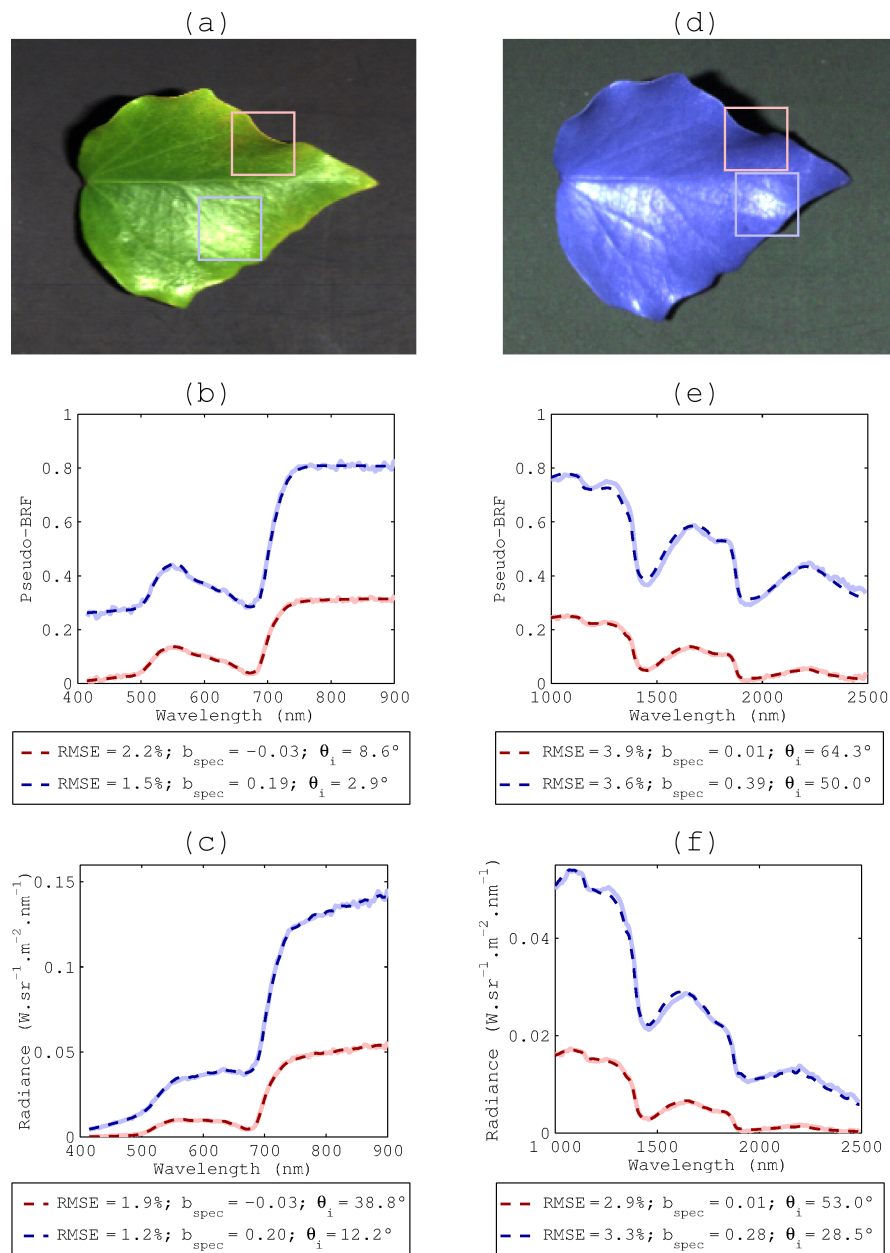


Figure 4: Fitting results obtained for the VNIR range (a-c) and the SWIR range (d-f) using the pseudo-BRF model (b,e) and the radiance model (c,f). Solid (resp. dashed) lines correspond to measurements (resp. simulations). Blue curves correspond to areas strongly affected by specular reflection, while red curves correspond to areas characterized by a high incident angle.

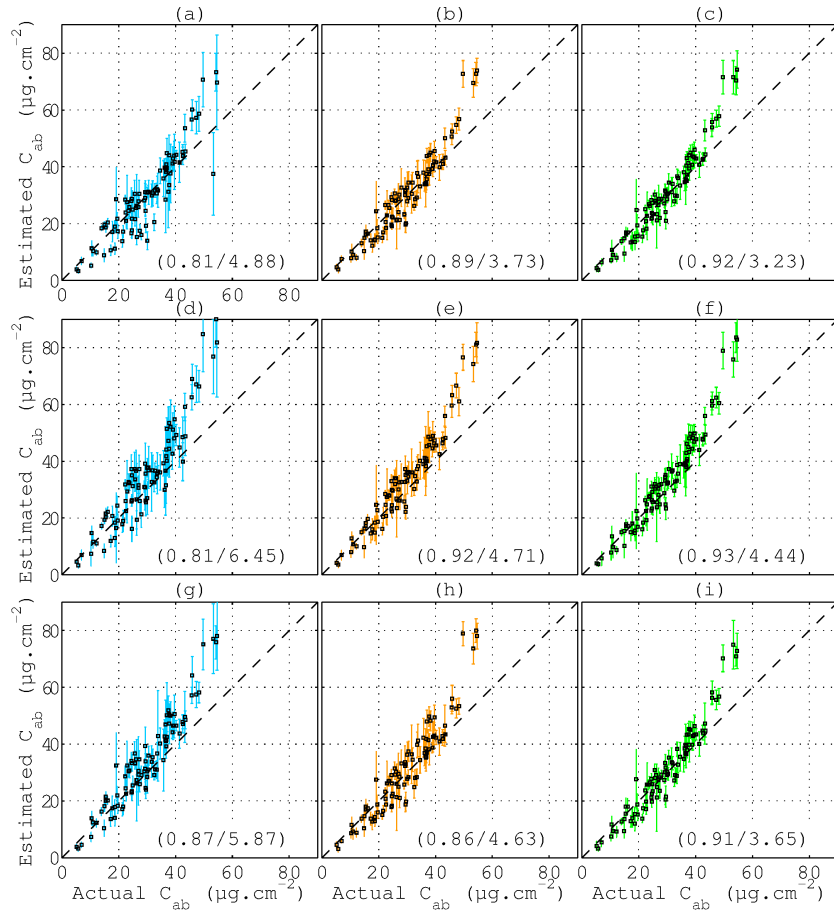


Figure 5:  $C_{ab}$  estimation results (mean  $\pm$  standard deviation) obtained with PROSPECT (blue), the pseudo-BRF based PROCOSINE model (orange), and the radiance-based PROCOSINE model (green) and with  $\bar{\theta}_i = 20^\circ$  (a-c),  $\bar{\theta}_i = 0^\circ$  (d-f) and  $\bar{\theta}_i = 40^\circ$  (g-i). The  $R^2$  and RMSE values are computed for actual  $C_{ab}$  values lower than  $40 \mu\text{g}\cdot\text{cm}^{-2}$  and are given in parentheses.



509 *4.2.2. Results of parameter retrievals in the VNIR range*

510 As recalled by the sensitivity analysis, the VNIR reflectance is mainly  
511 driven by the chlorophyll a+b content. In Fig. 5, we show the means and  
512 standard deviations of  $C_{ab}$  estimation obtained for each leaf disk with leaves  
513 in horizontal position (Figure 5.a-c) and tilted position (Figure 5.d-i). We  
514 compare the results obtained with PROSPECT (in blue), the pseudo-BRF  
515 based PROCOSINE model (in orange) and the radiance-based PROCOSINE  
516 model (in green). Because of the saturation in the reference measurement  
517 (see Section 3.1.2), the RMSE and  $R^2$  values were computed from samples  
518 for which the measured  $C_{ab}$  values were lower than  $40 \mu\text{g.cm}^{-2}$ .

519

520 On average, when tested with horizontal leaves, the radiance-based PRO-  
521 COSINE model led to a higher accuracy ( $R^2 = 0.92$ ;  $\text{RMSE} = 3.23 \mu\text{g.cm}^{-2}$ )  
522 than the pseudo-BRF PROCOSINE model ( $R^2 = 0.89$ ;  $\text{RMSE} = 3.73 \mu\text{g.cm}^{-2}$ )  
523 and PROSPECT ( $R^2 = 0.81$ ;  $\text{RMSE} = 4.88 \mu\text{g.cm}^{-2}$ ). Applying the same  
524 models to leaves in tilted position decreased the estimation accuracy, how-  
525 ever to a variable extent. For  $\bar{\theta}_i = 0^\circ$ , the radiance-based PROCOSINE  
526 model ( $R^2 = 0.93$ ;  $\text{RMSE} = 4.44 \mu\text{g.cm}^{-2}$ ) still performed better than the  
527 pseudo-BRF based PROCOSINE model ( $R^2 = 0.92$ ;  $\text{RMSE} = 4.71 \mu\text{g.cm}^{-2}$ )  
528 and PROSPECT ( $R^2 = 0.81$ ;  $\text{RMSE} = 6.45 \mu\text{g.cm}^{-2}$ ). The same trend was  
529 also observed for  $\bar{\theta}_i = 40^\circ$ , the radiance-based PROCOSINE model leading  
530 to a better accuracy ( $R^2 = 0.91$ ;  $\text{RMSE} = 3.65 \mu\text{g.cm}^{-2}$ ) than the pseudo-  
531 BRF based PROCOSINE model ( $R^2 = 0.86$ ;  $\text{RMSE} = 4.63 \mu\text{g.cm}^{-2}$ ) and  
532 PROSPECT ( $R^2 = 0.87$ ;  $\text{RMSE} = 5.87 \mu\text{g.cm}^{-2}$ ).

533 Overall, both PROCOSINE implementations obtained significantly lower

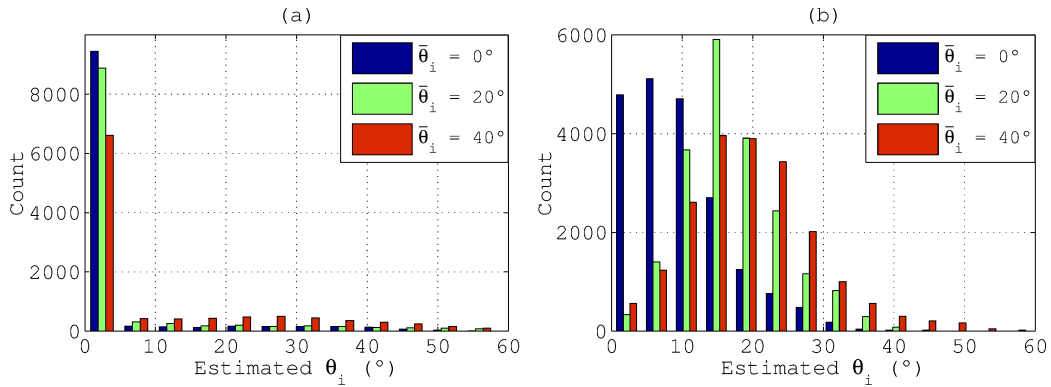


Figure 6: Histograms of estimated  $\theta_i$  values for every pixel for the VNIR range and the three acquisition configurations ( $\bar{\theta}_i = 0^\circ$ ,  $\bar{\theta}_i = 20^\circ$ , and  $\bar{\theta}_i = 40^\circ$ ): (a) pseudo-BRF based PROCOSINE model, and (b) radiance-based PROCOSINE model.

534 standard deviations of  $C_{ab}$  estimation than PROSPECT.

535 Lastly, for  $C_{ab} > 40 \mu\text{g}\cdot\text{cm}^{-2}$ , model inversion always provided higher  $C_{ab}$   
536 values than those measured with the Dualex.

537

538 The incident angle estimation within the whole leaves is evaluated in  
539 Fig. 6. The results are presented using histograms to account for within-leaf  
540 variability of leaf orientation. For both model implementations, we represent  
541 the distributions of  $\theta_i$  values estimated for every pixel for the three acquisition  
542 configurations (i.e., average incident angles  $\bar{\theta}_i$  of  $0^\circ$ ,  $20^\circ$ , and  $40^\circ$ ).

543 Surprisingly, strong differences were observed between both model inversions.  
544 On the one hand, the pseudo-BRF based model gave poor estimation results  
545 with estimated  $\bar{\theta}_i$  of  $3.3^\circ$ ,  $5.1^\circ$  and  $11.7^\circ$  (and the same estimated distribution  
546 mode, i.e.,  $2.4^\circ$ ) for  $\bar{\theta}_i = 0^\circ$ ,  $\bar{\theta}_i = 20^\circ$ , and  $\bar{\theta}_i = 40^\circ$  respectively. On the other  
547 hand, the radiance-based model gave better estimation results with estimated  
548  $\bar{\theta}_i$  of  $9.7^\circ$ ,  $16.9^\circ$  and  $19.6^\circ$  (and estimated distribution modes of  $6.3^\circ$ ,  $14.8^\circ$

549 and  $14.8^\circ$ ) for  $\bar{\theta}_i = 0^\circ$ ,  $\bar{\theta}_i = 20^\circ$ , and  $\bar{\theta}_i = 40^\circ$  respectively.

550 It is worth noting that poorer angle estimation results were generally obtained  
551 for bamboo leaves (results not shown) with estimated distribution modes of  
552  $15.4^\circ$ ,  $28.6^\circ$  and  $28.6^\circ$ ) for  $\bar{\theta}_i = 0^\circ$ ,  $\bar{\theta}_i = 20^\circ$ , and  $\bar{\theta}_i = 40^\circ$  respectively.

#### 553 *4.2.3. Results of parameter retrievals in the SWIR range*

554 Regarding PROSPECT original parameters, variation in SWIR reflectance  
555 is mainly produced by variation in equivalent water thickness, leaf mass per  
556 area and leaf structure.

557 In Fig. 7, we show the means and standard deviations of  $C_w$  estimation  
558 obtained with leaves in horizontal position (Fig. 7.a-c) and in tilted posi-  
559 tion (Fig. 7.d-i). For horizontal leaves, PROCOSINE performed better than  
560 PROSPECT in terms of  $R^2$  ( $R^2 = 0.91$  for PROSPECT,  $R^2 = 0.93$  for  
561 the pseudo-BRF based PROCOSINE model and  $R^2 = 0.94$  for the radiance-  
562 based PROCOSINE model), but worse in terms of RMSE (RMSE = 0.0016 cm,  
563 RMSE = 0.0083 cm and RMSE = 0.0025 cm resp.). However, the PRO-  
564 COSINE performances remained mostly unchanged when applied to tilted  
565 leaves, while PROSPECT obtained poorer performances, either for  $\bar{\theta}_i = 10^\circ$   
566 (a 125% increase in RMSE) or  $\bar{\theta}_i = 50^\circ$  (a 15% decrease in  $R^2$ ).

567 The RMSE values obtained with PROCOSINE were primarily due to a sys-  
568 tematic bias, the  $R^2$  values being higher than 0.91 for the three acquisition  
569 configurations. This bias was more pronounced for the pseudo-BRF based  
570 model, and led to a systematic overestimation of  $C_w$ .

571 Lastly, similarly to  $C_{ab}$  estimation, PROCOSINE obtained lower standard  
572 deviations of  $C_w$  estimation than PROSPECT, especially for tilted leaves.

573

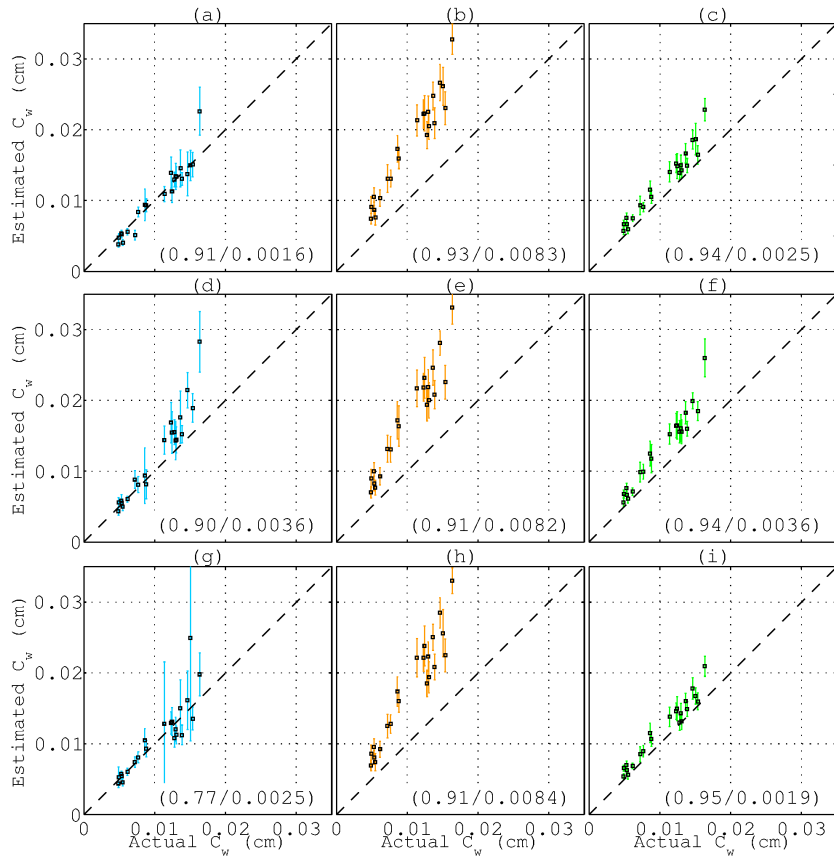


Figure 7:  $C_w$  estimation results (mean +/- standard deviation) obtained with PROSPECT (blue), the pseudo-BRF based PROCOSINE model (orange), and the radiance-based PRO-COSINE model (green) and with  $\bar{\theta}_i = 30^\circ$  (a-c),  $\bar{\theta}_i = 10^\circ$  (d-f) and  $\bar{\theta}_i = 50^\circ$  (g-i).  $R^2$  and RMSE values are given in parentheses.

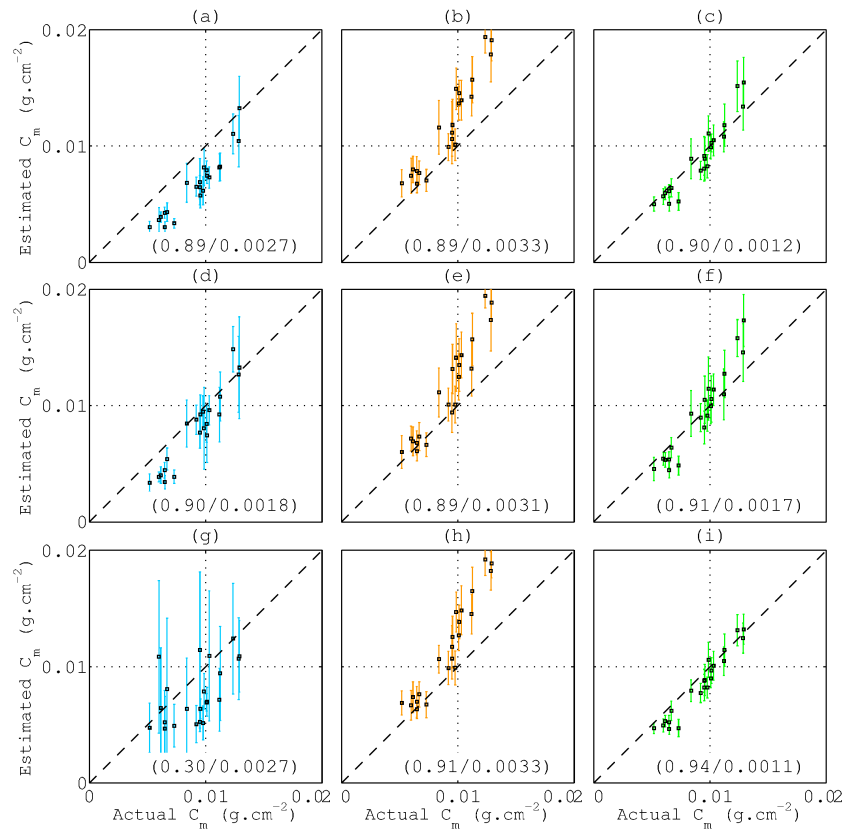


Figure 8:  $C_m$  estimation results (mean  $\pm$  standard deviation) obtained with PROSPECT (blue), the pseudo-BRF based PROCOSINE model (orange), and the radiance-based PROCOSINE model (green) and with  $\bar{\theta}_i = 30^\circ$  (a-c),  $\bar{\theta}_i = 10^\circ$  (d-f) and  $\bar{\theta}_i = 50^\circ$  (g-i).  $R^2$  and RMSE values are given in parentheses.

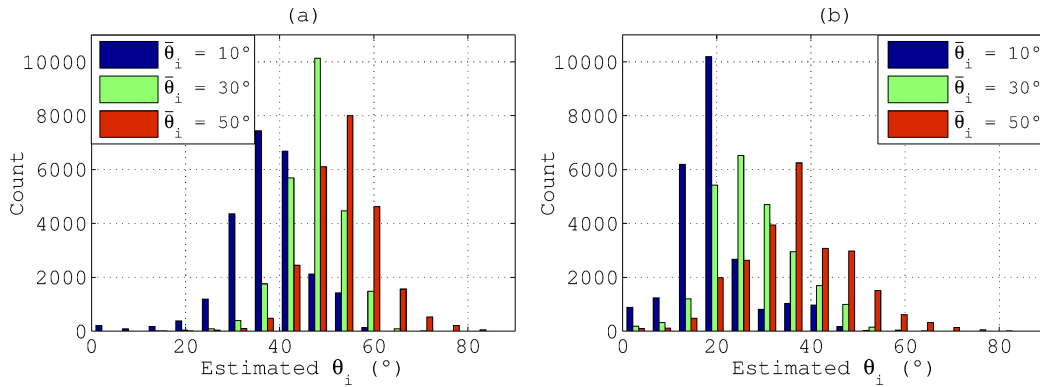


Figure 9: Histograms of estimated  $\theta_i$  values in every pixel for the SWIR range and the three acquisition configurations ( $\bar{\theta}_i = 10^\circ$ ,  $\bar{\theta}_i = 30^\circ$ , and  $\bar{\theta}_i = 50^\circ$ ): (a) pseudo-BRF based PROCOSINE model, and (b) radiance-based PROCOSINE model.

574 The  $C_m$  retrieval results are presented in Fig. 8 in a similar fashion to  $C_w$ .  
 575 The radiance-based PROCOSINE model gave significantly lower RMSE than  
 576 the pseudo-BRF based PROCOSINE model and PROSPECT, i.e., RMSE =  
 577  $0.0013 \text{ g.cm}^{-2}$ , RMSE =  $0.0032 \text{ g.cm}^{-2}$ , and RMSE =  $0.0024 \text{ g.cm}^{-2}$  respec-  
 578 tively on average for the three acquisition configurations. The PROCOSINE  
 579 performances weakly depended on leaf position, whereas the  $R^2$  dropped  
 580 from 0.89 for  $\bar{\theta}_i = 10^\circ$  and  $\bar{\theta}_i = 30^\circ$ , to 0.30 for  $\bar{\theta}_i = 50^\circ$  when inverting only  
 581 PROSPECT. For such high incident angles, the uncertainty of  $C_m$  estimation  
 582 was much higher with PROSPECT than with PROCOSINE.  
 583 Lastly,  $C_m$  was generally underestimated by PROSPECT and overestimated  
 584 by the pseudo-BRF based PROCOSINE model.

585

586 The two PROCOSINE inversions were also compared based on  $\theta_i$  esti-  
 587 mation results in Fig. 9, in which we represent the histograms of estimated  
 588  $\theta_i$  distributions. As expected, in both cases, the highest (resp. the lowest)

589 angles were mostly retrieved from the  $\bar{\theta}_i = 50^\circ$  (resp.  $\bar{\theta}_i = 10^\circ$ ) configuration,  
590 the dispersions around the mean values being due to the variation in leaf ori-  
591 entation.  $\theta_i$  was more accurately predicted using the radiance-based model  
592 since the estimated  $\bar{\theta}_i$  were  $19.7^\circ$ ,  $27.7^\circ$  and  $36.4^\circ$  for  $\bar{\theta}_i = 10^\circ$ ,  $\bar{\theta}_i = 30^\circ$ , and  
593  $\bar{\theta}_i = 50^\circ$  respectively. The pseudo-BRF based model globally overestimated  
594  $\theta_i$  since the estimated  $\bar{\theta}_i$  were  $38.0^\circ$ ,  $47.2^\circ$  and  $53.0^\circ$  for  $\bar{\theta}_i = 10^\circ$ ,  $\bar{\theta}_i = 30^\circ$ ,  
595 and  $\bar{\theta}_i = 50^\circ$  respectively.

596 Similarly to the VNIR range, poorer estimation results were generally ob-  
597 tained for bamboo leaves (results not shown). For example, the radiance-  
598 based model led to estimated  $\bar{\theta}_i$  of  $38.0^\circ$ ,  $43.4^\circ$  and  $47.0^\circ$  for  $\bar{\theta}_i = 10^\circ$ ,  $\bar{\theta}_i = 30^\circ$ ,  
599 and  $\bar{\theta}_i = 50^\circ$  respectively.

#### 600 4.2.4. Discussion about parameter retrievals

601 *Estimation of chlorophyll content.* In the VNIR range, both PROCOSINE  
602 implementations performed better than PROSPECT in retrieving  $C_{ab}$ . For  
603 leaves in horizontal position, the 34% improvement in RMSE when using the  
604 radiance-based PROCOSINE model instead of PROSPECT is likely to be  
605 due mainly to the modeling of BRDF effects. Not taking them into account  
606 leads to a greater uncertainty as shown through the estimation standard devi-  
607 ations computed within each leaf disk. For example, as illustrated in Fig. 5.a  
608 with the sample corresponding to an actual mean value of  $53 \mu\text{g}\cdot\text{cm}^{-2}$ , a  
609 local BRDF effect induces an overall increase in reflectance, which is misin-  
610 terpreted by PROSPECT as a decrease in  $C_{ab}$ . This result confirms one of the  
611 conclusions drawn from the sensitivity analysis, which has already showed  
612 that  $b_{spec}$  significantly affects leaf close-range hyperspectral measurements.

613 The difference between PROCOSINE and PROSPECT was even greater

614 when considering leaves in tilted position, for which the modeling of leaf  
615 inclination was more important. In particular, for the highest incident angle  
616 ( $\bar{\theta}_i = 40^\circ$ ), both the modeling of BRDF effects and leaf orientation within  
617 the radiance-based PROCOSINE model led to an actual 38% improvement  
618 over PROSPECT. It is worth noting that taking  $\theta_i$  into account improves  
619 the  $C_{ab}$  estimation results even if  $C_{ab}$  is mainly retrieved between 400 and  
620 750 nm, in which the effect of  $\theta_i$  is lower (see Fig. 3.c). In fact, the difference  
621 in retrieval performance in VNIR between PROSPECT and PROCOSINE is  
622 even greater for  $N$  leaf structure parameter that mainly affects reflectance  
623 in the NIR plateau, where both  $\theta_i$  and  $b_{spec}$  have a strong influence on re-  
624 flectance ( $N$  maps are only shown for the SWIR range, see Fig. 12).

625 The PROCOSINE inversion performed well compared with the accuracy pro-  
626 vided by the Dualex manufacturer, i.e.,  $RMSE = 5 \mu\text{g}\cdot\text{cm}^{-2}$  (Cerovic et al.,  
627 2012), especially considering that spectral measurements are affected by ex-  
628 tra variability and that the method is based on reflectance, which is known to  
629 be less sensitive to  $C_{ab}$  than transmittance (Baret & Fourty, 1997b). Import-  
630 tantly, the apparent  $C_{ab}$  overestimation for  $C_{ab} > 40 \mu\text{g}\cdot\text{cm}^{-2}$  was rather due  
631 to the saturation in the reference measurement (see Section 3.1.2), as also  
632 suggested by the similar trend observed for both PROSPECT and PRO-  
633 COSINE. Further experiments conducted on hyperspectral data associated  
634 with laboratory extraction based measurements of pigment contents (includ-  
635 ing  $C_{cx}$ ) would, however, be interesting to fully characterize the pigment  
636 retrieval.

637 The main difference between both PROCOSINE inversions arose for high  
638 incident angles, since the RMSE decreased by 21% when using the radiance-



639 based model. This result confirms that this implementation better handles  
640 variation in leaf orientation as displayed in Fig. 6.

641 *Estimation of equivalent water thickness and leaf mass per area.* Somewhat  
642 different observations could be made from the SWIR range. In most cases,  
643 the retrievals of  $C_w$  and  $C_m$  resulted in lower RMSE when using the radiance-  
644 based PROCOSINE model. In particular, the  $C_m$  estimation was very accu-  
645 rate even if  $C_m$  is not the most influential parameter in this spectral domain  
646 (see Fig. 3.d). The poor  $R^2$  value and very high standard deviations obtained  
647 with PROSPECT and  $\bar{\theta}_i = 50^\circ$  again demonstrate the need for accounting  
648 for BRDF effects and leaf orientation, especially when the targeted parame-  
649 ter does not have a strong influence on reflectance.

650

651 However, as recalled in Section 2.2.1, BRDF effects are not properly taken  
652 into account for the SWIR range because, unlike the VNIR range,  $b_{spec}$  de-  
653 pends on wavelength. Indeed, the BRDF directional component depends on  
654 the leaf refractive index (Bousquet et al., 2005), whose imaginary part is  
655 proportional to absorption (Born & Wolf, 1980). Especially at the far end  
656 of the SWIR range, water absorption is so strong (Hale & Querry, 1973)  
657 that the imaginary part of the leaf refractive index is no longer negligible  
658 compared with the real part (Gerber et al., 2011). This may explain why  
659 PROSPECT is more accurate than PROCOSINE in retrieving  $C_w$  on leaves  
660 in horizontal position. Presumably, PROCOSINE systematically overesti-  
661 mates  $C_w$  to mimic the decrease of the leaf refractive index (Féret et al.,  
662 2008). The compensation between  $C_w$  and  $b_{spec}$  allows the proposed models  
663 to be adjusted to the SWIR range and to obtain better estimation results

664 for other PROSPECT parameters such as  $C_m$ . For leaves in tilted position,  
665 the influence of leaf orientation, whose modeling does not depend on wave-  
666 length, again makes the radiance-based PROCOSINE model more accurate  
667 than PROSPECT.

668

669 Importantly, the high  $R^2$  values obtained with PROCOSINE for  $C_w$  and  
670  $C_m$  retrievals make it possible to calibrate strong linear relationships between  
671 the actual values and the estimated values. Indeed, in every case, the ob-  
672 tained RMSE is driven more by the estimation bias than by the variance. As  
673 carried out by Cheng et al. (2011), applying such an indirect retrieval could  
674 correct this bias and significantly enhance the estimation results obtained  
675 with a given experimental setup.

676 *Angle estimation.* Both in the VNIR and SWIR ranges, the performances of  
677 PROCOSINE weakly depended on leaf position. This tends to prove that  
678 non-regular surfaces can be handled properly by introducing the  $\theta_i$  parame-  
679 ter. However, some clear differences arose between pseudo-BRF and radiance  
680 inversions. Overall, inverting the radiance-based model provided the best re-  
681 sults, the strongest difference between both ranges lying in  $\theta_i$  estimation,  
682 especially in the VNIR range.  $\theta_i$  was indeed better retrieved using radiance-  
683 based inversion, the  $\theta_i$  underestimation for high incident angles and both  
684 ranges being presumably due to the assumption  $\frac{1-\rho_{spec}(\theta_i;2\pi)}{1-\rho_{spec}(0;2\pi)} \approx 1$  in Eq. 20.  
685 It could be shown that confounding effects between  $\theta_i$  and  $N$  (as well as  $C_m$   
686 in the VNIR range) were responsible for poor  $\theta_i$  estimation results obtained  
687 through pseudo-BRF inversion. For example, as observed in Fig. 3, both  $\theta_i$   
688 and  $N$  have similar contributions to the model output. However, they also

689 have opposite effects, which may lead the inversion process to misinterpret  
690 an increase in  $\theta_i$  as a decrease in leaf structure  $N$ . Therefore, in the VNIR  
691 (resp. SWIR) range, this model compensates  $\theta_i$  underestimation (overesti-  
692 mation) by  $N$  underestimation (overestimation).

693 On the other hand, several assumptions can be made regarding the good  
694 performances obtained by radiance-based inversion. First, this may be due  
695 to the noise level in the spectral measurements: as the ratio of two radi-  
696 ance spectra is noisier than both radiance spectra independently, retrieved  
697 pseudo-BRF spectra thus have a lower signal-to-noise ratio than originally  
698 measured radiance spectra. This problem is critical near 400 nm and in the  
699 NIR plateau where the sensitivity of the VNIR camera is lower compared  
700 with most of the visible range (see Fig. 4). This emphasizes the necessity  
701 of acquiring spectral measurements as clean as possible. Alternatively, such  
702 differences in the inversion performances may be due to the numerical imple-  
703 mentation of the inversion process (e.g., through the considered cost function,  
704 optimization algorithm or initialization). Further investigation is therefore  
705 needed to fully optimize the PROCOSINE inversion.

706

707 Finally, the poorer angle estimation results obtained with bamboo leaves  
708 were likely to be due to the azimuthally anisotropic roughness properties of  
709 monocotyledon leaves, that mainly originate from the longitudinal orienta-  
710 tion of veins (Comar et al., 2012, 2014). Unlike regular surfaces for which  
711 the BRF is azimuthally symmetric, such an organized arrangement of the  
712 leaf surface leads the specular lobe not to be in the principal plane (Miesch  
713 et al., 2002). In this case, it may seem inappropriate to represent the local

714 leaf inclination at the pixel level using only a single mean angle, especially  
715 because the image spatial resolution is comparable to the inter-vein distance  
716 for monocotyledons, i.e., a few hundred micrometers (Comar et al., 2014).  
717 However, other estimation results presented in this paper strongly suggest  
718 that this does not affect the retrievals of leaf biochemical properties.

#### 719 *4.3. Leaf parameter mapping*

720 Hyperspectral imaging allowed us to obtain high-resolution maps of model  
721 parameters by inverting the model for each pixel. Compared with the results  
722 obtained from estimated values averaged within one or several leaf disk(s)  
723 (each of which contains several hundreds of pixels), such maps provide a  
724 deeper insight in how these effects actually affect the estimation process.

725 In Fig. 10 and Fig. 11, we show some estimated maps obtained using PROSPECT  
726 and the radiance-based PROCOSINE model respectively, the radiance-based  
727 inversion performing better than the pseudo-BRF inversion as seen in Sec-  
728 tion 4.2. The considered bay laurel leaf was chosen due to its strong non  
729 Lambertian behavior and to the presence of a large range of  $C_{ab}$  and  $C_{bp}$   
730 values. The actual chlorophyll content in the greenest area was close to  
731  $40 \mu\text{g}\cdot\text{cm}^{-2}$ , while the equivalent water thickness and leaf mass per area were  
732  $0.0088 \text{ cm}$  and  $0.0099 \text{ g}\cdot\text{cm}^{-2}$  respectively.

733 On the one hand, as observed in Fig. 10, PROSPECT estimation was strongly  
734 affected by BRDF effects both in the VNIR and SWIR ranges. This increase  
735 in reflectance is not taken into account by PROSPECT, which resulted in  
736 some compensations during the inversion, here corresponding to an increase  
737 in  $C_{bp}$  and decreases in  $C_{ab}$  (as already mentioned in Section 4.2.2),  $C_w$  and  
738  $C_m$ . On the other hand, in Fig. 11, we show that these BRDF effects were

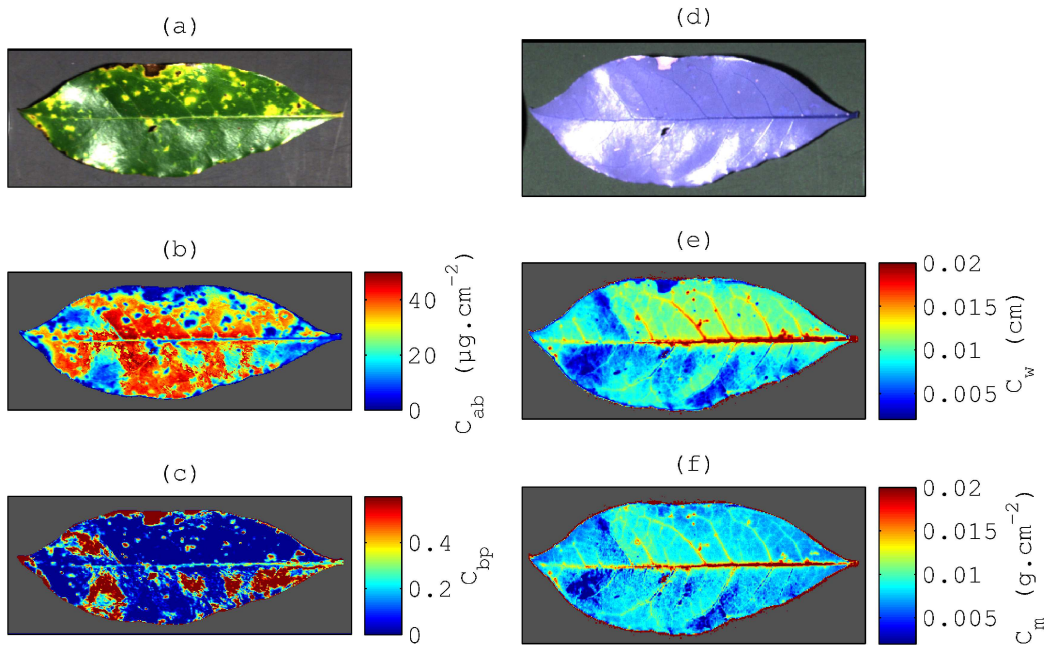


Figure 10: Estimated maps obtained using PROSPECT in the VNIR (a-c) and SWIR (d-f) ranges: (a) true color composite image, (b)  $C_{ab}$ , (c)  $C_{bp}$ , (d) false color composite image (using bands 1458 nm, 2202 nm and 1662 nm), (e)  $C_w$ , (f)  $C_m$ .

739 correctly interpreted as local increases in  $b_{spec}$  within the PROCOSINE in-  
 740 version. Accurate descriptions of the actual regular leaf orientation were also  
 741 obtained through homogeneous  $\theta_i$  maps and average  $\theta_i$  of  $15^\circ$  and  $30^\circ$  for the  
 742 VNIR and SWIR ranges respectively.

743 Modeling such extra variability therefore allowed us to obtain consistent maps  
 744 of foliar content. In the VNIR range, the highest  $C_{ab}$  values were obtained  
 745 in the greenest parts with values close to  $40 \mu\text{g}\cdot\text{cm}^{-2}$ , while very low chloro-  
 746 phyll contents were retrieved in senescent parts, especially in the necrotic  
 747 area on the top (Fig. 11.b). This latter area was also exhibiting a high con-  
 748 tent in brown pigments as shown in Fig. 11.c, thereby proving the reliability

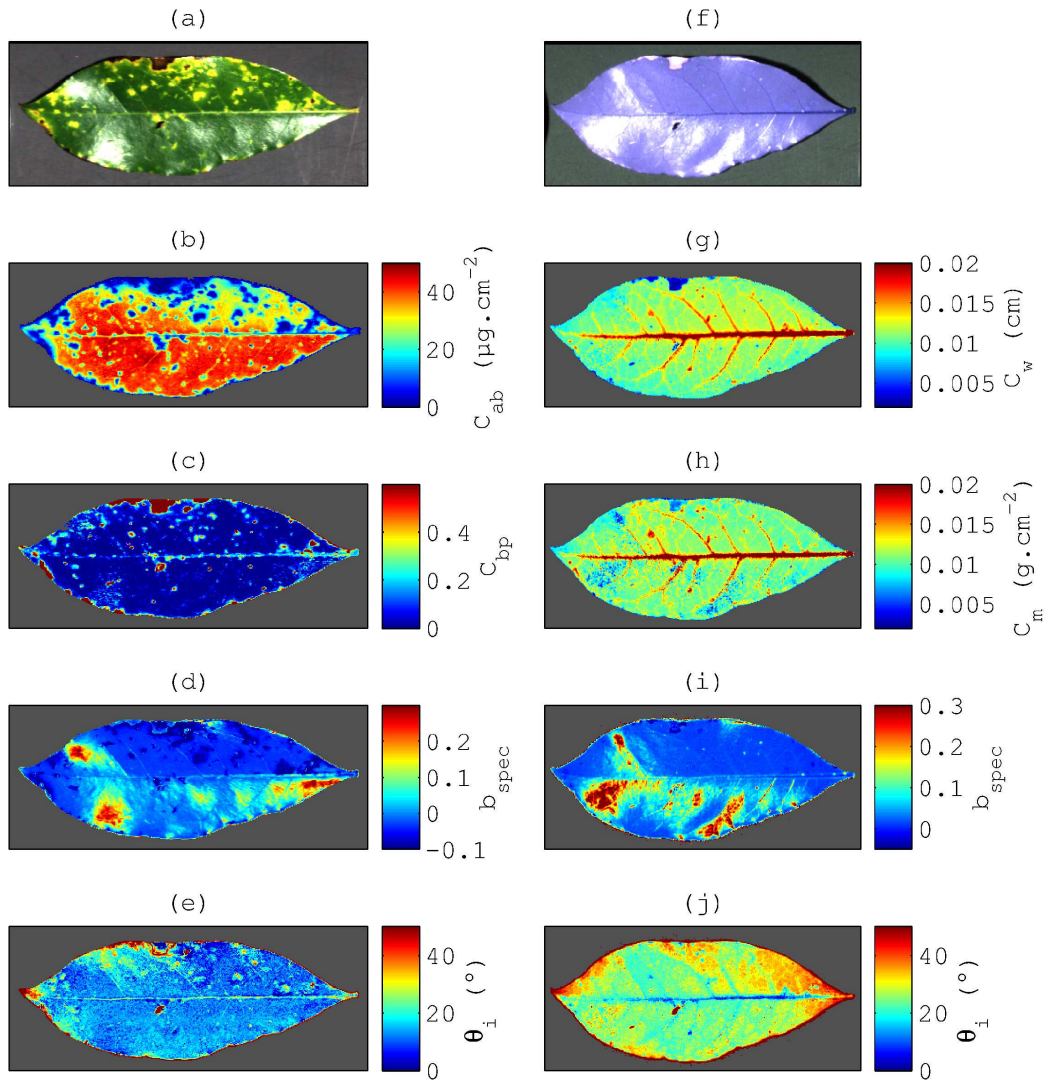


Figure 11: Estimated maps obtained using the radiance-based PROCOSINE model in the VNIR (a-e) and SWIR (f-j) ranges: (a) true color composite image, (b)  $C_{ab}$ , (c)  $C_{bp}$ , (d)  $b_{spec}$ , (e)  $\theta_i$ , (f) false color composite image (using bands 1458 nm, 2202 nm and 1662 nm), (g)  $C_w$ , (h)  $C_m$ , (i)  $b_{spec}$ , (j)  $\theta_i$ .

749 of PROSPECT for retrieving pigments.

750 Consistent maps were obtained in the SWIR range as well. As expected,  
751 veins were found to contain a lot of water, unlike the upper part where  
752 necrosis was causing a strong water loss (Fig. 11.g). Although being a bit  
753 more affected than  $C_w$  by mismodeled BRDF effects,  $C_m$  was estimated more  
754 accurately than  $C_w$  since both  $C_w$  and  $C_m$  average estimated values were close  
755 to  $0.011 \text{ g.cm}^{-2}$ .

756 In particular, these maps are very appealing for identifying plant diseases at  
757 leaf scale. As described by Mahlein et al. (2013), different diseases may lead  
758 to different symptoms that can be characterized by local changes in optical  
759 properties, e.g., a higher chlorophyll/carotenoid ratio for sugar beet rust, or  
760 necrosis for *Cercospora* leaf spot. Therefore, inverting PROCOSINE based  
761 on VNIR and SWIR hyperspectral images of the same leaf offers very inter-  
762 esting perspectives for early detection of many plant diseases.

763

764 Finally, in Fig. 12, we provide a last example that again demonstrates the  
765 potential of PROCOSINE in the SWIR range when tested with a sugar beet  
766 leaf characterized by high  $C_w$  ( $C_w = 0.0355 \text{ cm}$ ) and low  $C_m$  ( $C_m = 0.0040 \text{ g.cm}^{-2}$ )  
767 values, and by a strongly non-regular and non-Lambertian leaf surface. Even  
768 if PROSPECT obtained better results when considering estimated values av-  
769 eraged over the five sampled leaf disks ( $\hat{C}_w = 0.0370 \text{ cm}$ ;  $\hat{C}_m = 0.0032 \text{ g.cm}^{-2}$ ),  
770 it also led to highly heterogeneous and inconsistent maps, whose variances  
771 obviously did not reflect the actual ones but rather expressed unmodelled  
772 variability. Conversely, the PROCOSINE inversion led to homogeneous and  
773 consistent maps, either for leaf structure ( $\hat{N} = 1.30$ ; to compare with



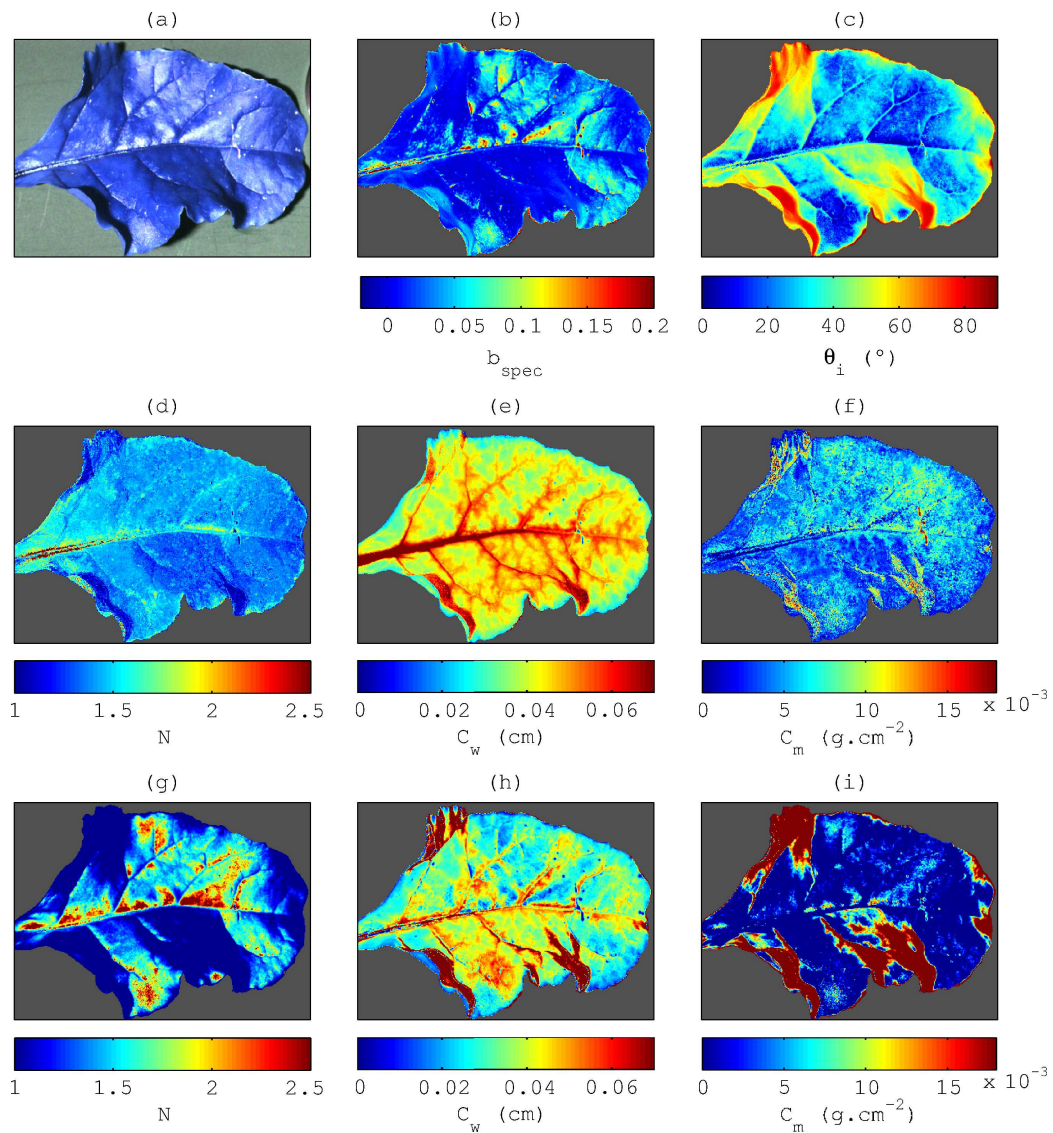


Figure 12: Estimated maps obtained in the SWIR range using the radiance-based PRO-COSINE model (b-f) and PROSPECT (g-i): (a) false color composite image (using bands 1458 nm, 2202 nm and 1662 nm), (b)  $b_{spec}$ , (c)  $\theta_i$ , (d)  $N$ , (e)  $C_w$ , (f)  $C_m$ , (g)  $N$ , (h)  $C_w$ , (i)  $C_m$ .



774 the mean value of 1.225 provided by Jacquemoud et al. (1996) for the same  
775 species), equivalent water thickness ( $\widehat{C}_w = 0.042$  cm) and leaf mass per area  
776 ( $\widehat{C}_m = 0.0052$  g.cm<sup>-2</sup>). In particular, the strongly non regular leaf orienta-  
777 tion was greatly retrieved through the estimated  $\theta_i$  map (Fig. 12.c): regions  
778 with low estimated  $\theta_i$  were indeed facing the light source while regions with  
779 high estimated  $\theta_i$  were facing the opposite side (note that shadows were inter-  
780 preted as high  $\theta_i$  values). Interestingly, most imaging techniques allowing the  
781 retrieval of leaf (or even plant) orientation are either based on depth imaging  
782 systems (Chéné et al., 2012) or on 3D models built from multi-angular obser-  
783 vations using stereovision (Lati et al., 2013) or photogrammetry (Jay et al.,  
784 2015). In comparison, it is worth noting that in this study, the retrieval of  
785 leaf orientation only necessitates a single-angular observation and is based  
786 on spectral information only.

## 787 5. Conclusions and perspectives

788 In this study, we propose a physically-based model that allows for ap-  
789 plying rigorously a DHR model of leaf optical properties to pseudo-BRF  
790 hyperspectral (or multispectral) images acquired with close-range imaging  
791 spectroscopy. The proposed COSINE model describes the spectral variabil-  
792 ity caused by variable BRDF effects and leaf orientation, that, depending  
793 on leaf surface, can make the acquired pseudo-BRF measurements very dif-  
794 ferent from DHR measurements. In this paper, COSINE is coupled with  
795 PROSPECT and the numerical inversion of the resulting PROCOSINE model  
796 led to accurate leaf-level mappings of foliar content and above leaf surface  
797 properties, both in the VNIR and SWIR ranges.

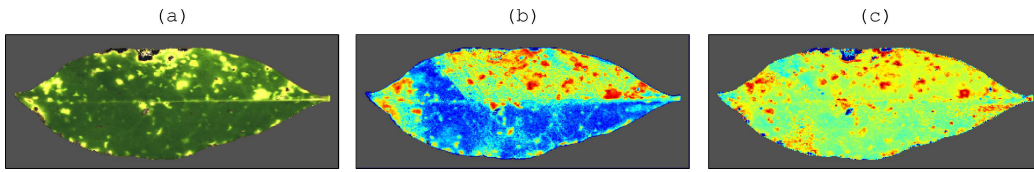


Figure 13: Use of the PROCOSINE model for image pretreatment in the VNIR (a-c) range: (a) DHR image reconstructed with PROSPECT and estimated parameters, (b) *SBRI* map (Mahlein et al., 2013) obtained with the original image, and (c) *SBRI* map (Mahlein et al., 2013) obtained with the reconstructed image.

798 Besides avoiding the need for hemispherical measurements, the proposed ap-  
799 proach allows the non-destructive biochemical characterization of small leaves  
800 thanks to the sub-millimeter resolution of hyperspectral images. Potentially,  
801 it could represent a practical solution for optical characterization of needles,  
802 whose optical properties were found to be well described by PROSPECT  
803 (Moorthy et al., 2008) (usual needle optical measurements involving using  
804 complex experimental setups to handle irregularities in size, shape and cur-  
805 vature). As previously mentioned, it can also be combined with other leaf  
806 DHR models such as LIBERTY (Dawson et al., 1998).

807 The accurate retrieval of  $C_m$  makes it possible to derive mass-based quantities  
808 from surface-based quantities. In particular, strong correlations ( $R^2 > 0.85$ )  
809 were obtained for the estimation of Gravimetric Water Content (being ex-  
810 pressed as  $C_w/C_m$ ), which is an important indicator for fire risk modeling  
811 (Chuvieco et al., 2004).

812 Potential applications also include the use of PROCOSINE as a pretreat-  
813 ment for further processing. To illustrate, in Fig. 13.a, we show a DHR  
814 image reconstructed by running PROSPECT in a forward mode with pa-  
815 rameters previously estimated with the radiance-based PROCOSINE model

816 (the original image is presented in Fig. 10). For example, computing spectral  
817 indices designed for plant disease identification based on this cleaned image  
818 is much more reliable to detect these diseases at early infection stages, es-  
819 pecially when these indices are based on wavelengths strongly affected by  
820 BRDF effects, e.g., the SBRI (Mahlein et al., 2013). Alternatively, PRO-  
821 COSINE could allow the design of spectral indices adapted to close-range  
822 imaging spectroscopy, similarly to F eret et al. (2011).  
823 Further investigation is however needed to properly model the specular com-  
824 ponent in the SWIR range. In this case, the effect of water absorption on  
825 leaf refractive index should be considered to reliably model the wavelength-  
826 dependency of  $b_{spec}$  parameter. Also, confounding effects between PROCOSINE  
827 parameters (e.g.,  $N$ ,  $\theta_i$  and  $C_m$  in the VNIR range) should be studied  
828 more deeply by optimizing the numerical implementation of the iterative op-  
829 timization or by considering regularization strategies as reviewed by Baret  
830 & Buis (2008) and Verrelst et al. (2015), e.g., by using prior knowledge to  
831 constrain some model variables, or by generating a look-up table and aver-  
832 aging the  $N$  best solutions. As noted in the discussion, a more exhaustive  
833 assessment of PROCOSINE should also be performed over a larger data set  
834 encompassing a wider range of pigment, water and dry matter contents prop-  
835 erly measured using laboratory extraction methods. This would allow us to  
836 fully validate the proposed model. Lastly, it is worth mentioning that the  
837 use of COSINE based on images acquired under outdoor conditions requires  
838 assuming that diffuse illumination (coming from either the sky and/or the  
839 surrounding terrain) is negligible compared with direct sunlight. We are  
840 currently working towards an improvement of COSINE to account for these

841 influences within the modeling, thus transforming the BRDF-based model into  
842 a hemispherical-directional reflectance factor based model. This would allow  
843 processing spatially-resolved data acquired from near-ground remote sensing,  
844 e.g., from a tower or low flying unmanned aerial vehicle.

## 845 **Acknowledgments**

846 This study was funded by the French National Research Agency, within  
847 the program "Investissements d'avenir" with the reference ANR-11-BTBR-  
848 0007 (AKER project). Many thanks to Xavier Briottet and the anonymous  
849 reviewers for their valuable comments and suggestions.

## 850 **References**

- 851 Ashikmin, M., Premoze, S., & Shirley, P. (2000). A microfacet-based BRDF  
852 generator. In *Proceedings of the 27th annual conference on Computer*  
853 *graphics and interactive techniques* (pp. 65–74). ACM Press/Addison-  
854 Wesley Publishing Co.
- 855 Bacour, C., Jacquemoud, S., Tourbier, Y., Dechambre, M., & Frangi, J.-P.  
856 (2002). Design and analysis of numerical experiments to compare four  
857 canopy reflectance models. *Remote Sensing of Environment*, 79, 72–83.
- 858 Bacour, C., Jacquemoud, S., Vogt, P., Hosgood, B., Andreoli, G., & Frangi,  
859 J.-p. (2001). Optimal sampling configurations for the estimation of canopy  
860 properties from BRDF data acquired with the EGO/JRC. In *Proc. 8th*  
861 *International Symposium Physical Measurements & Signatures in Remote*  
862 *Sensing* (pp. 481–486).

- 863 Baret, F., & Buis, S. (2008). Estimating canopy characteristics from remote  
864 sensing observations: Review of methods and associated problems. In  
865 S. Liang (Ed.), *Advances in Land Remote Sensing* (pp. 173–201). Springer  
866 Netherlands.
- 867 Baret, F., & Fourty, T. (1997a). Estimation of leaf water content and specific  
868 leaf weight from reflectance and transmittance measurements. *Agronomie*,  
869 *17*, 455–464.
- 870 Baret, F., & Fourty, T. (1997b). Radiometric estimates of nitrogen status of  
871 leaves and canopies. In G. Lemaire (Ed.), *Diagnosis of the Nitrogen Status*  
872 *in Crops* (pp. 201–227). Springer Berlin Heidelberg.
- 873 Blackburn, G. A. (2007). Hyperspectral remote sensing of plant pigments.  
874 *Journal of experimental botany*, *58*, 855–867.
- 875 Born, M., & Wolf, E. (1980). Chapter XIII - Optics of metals. In M. Born,  
876 & E. Wolf (Eds.), *Principles of Optics* (pp. 611 – 664). Pergamon. (Sixth  
877 (corrected) edition ed.).
- 878 Bousquet, L., Lachérade, S., Jacquemoud, S., & Moya, I. (2005). Leaf BRDF  
879 measurements and model for specular and diffuse components differentia-  
880 tion. *Remote Sensing of Environment*, *98*, 201–211.
- 881 Bowyer, P., & Danson, F. (2004). Sensitivity of spectral reflectance to varia-  
882 tion in live fuel moisture content at leaf and canopy level. *Remote Sensing*  
883 *of Environment*, *92*, 297–308.
- 884 Buddenbaum, H., & Hill, J. (2015). PROSPECT inversions of leaf laboratory

885 imaging spectroscopy—a comparison of spectral range and inversion tech-  
886 nique influences. *Photogrammetrie-Fernerkundung-Geoinformation*, 2015,  
887 231–240.

888 Cerovic, Z. G., Masdoumier, G., Ghazlen, N. B., & Latouche, G. (2012).  
889 A new optical leaf-clip meter for simultaneous non-destructive assessment  
890 of leaf chlorophyll and epidermal flavonoids. *Physiologia plantarum*, 146,  
891 251–260.

892 Chen, J., & Leblanc, S. (1997). A four-scale bidirectional reflectance model  
893 based on canopy architecture. *Geoscience and Remote Sensing, IEEE*  
894 *Transactions on*, 35, 1316–1337.

895 Chéné, Y., Rousseau, D., Lucidarme, P., Bertheloot, J., Caffier, V., Morel, P.,  
896 Belin, E., & Chapeau-Blondeau, F. (2012). On the use of depth camera for  
897 3D phenotyping of entire plants. *Computers and Electronics in Agriculture*,  
898 82, 122–127.

899 Cheng, T., Rivard, B., & Sanchez-Azofeifa, A. (2011). Spectroscopic deter-  
900 mination of leaf water content using continuous wavelet analysis. *Remote*  
901 *Sensing of Environment*, 115, 659–670.

902 Chuvieco, E., Cocero, D., Riano, D., Martin, P., Martinez-Vega, J., de la  
903 Riva, J., & Pérez, F. (2004). Combining NDVI and surface temperature  
904 for the estimation of live fuel moisture content in forest fire danger rating.  
905 *Remote Sensing of Environment*, 92, 322–331.

906 Colombo, R., Meroni, M., Marchesi, A., Busetto, L., Rossini, M., Giardino,  
907 C., & Panigada, C. (2008). Estimation of leaf and canopy water content in

- 908 poplar plantations by means of hyperspectral indices and inverse modeling.  
909 *Remote Sensing of Environment*, 112, 1820 – 1834.
- 910 Comar, A., Baret, F., Obein, G., Simonot, L., Meneveaux, D., Vinot, F., &  
911 de Solan, B. (2014). ACT: A leaf BRDF model taking into account the  
912 azimuthal anisotropy of monocotyledonous leaf surface. *Remote Sensing*  
913 *of Environment*, 143, 112 – 121.
- 914 Comar, A., Baret, F., Vinot, F., Yan, L., & de Solan, B. (2012). Wheat leaf  
915 bidirectional reflectance measurements: Description and quantification of  
916 the volume, specular and hot-spot scattering features. *Remote Sensing of*  
917 *Environment*, 121, 26 – 35.
- 918 Curran, P. J. (1989). Remote sensing of foliar chemistry. *Remote Sensing of*  
919 *Environment*, 30, 271 – 278.
- 920 Danson, F., & Bowyer, P. (2004). Estimating live fuel moisture content from  
921 remotely sensed reflectance. *Remote Sensing of Environment*, 92, 309–321.
- 922 Dawson, T. P., Curran, P. J., & Plummer, S. E. (1998). LIBERTY - modeling  
923 the effects of leaf biochemical concentration on reflectance spectra. *Remote*  
924 *Sensing of Environment*, 65, 50–60.
- 925 Dorigo, W., Zurita-Milla, R., de Wit, A., Brazile, J., Singh, R., & Schaep-  
926 man, M. (2007). A review on reflective remote sensing and data assim-  
927 ilation techniques for enhanced agroecosystem modeling. *International*  
928 *Journal of Applied Earth Observation and Geoinformation*, 9, 165 – 193.

- 929 Féret, J.-B., & Asner, G. P. (2014). Mapping tropical forest canopy diver-  
930 sity using high-fidelity imaging spectroscopy. *Ecological Applications*, *24*,  
931 1289–1296.
- 932 Féret, J.-B., François, C., Asner, G. P., Gitelson, A. A., Martin, R. E., Bidel,  
933 L. P., Ustin, S. L., le Maire, G., & Jacquemoud, S. (2008). PROSPECT-4  
934 and 5: Advances in the leaf optical properties model separating photosyn-  
935 thetic pigments. *Remote Sensing of Environment*, *112*, 3030–3043.
- 936 Féret, J.-B., François, C., Gitelson, A., Asner, G. P., Barry, K. M., Panigada,  
937 C., Richardson, A. D., & Jacquemoud, S. (2011). Optimizing spectral  
938 indices and chemometric analysis of leaf chemical properties using radiative  
939 transfer modeling. *Remote sensing of environment*, *115*, 2742–2750.
- 940 Gastellu-Etchegorry, J., Demarez, V., Pinel, V., & Zagolski, F. (1996). Mod-  
941 eling radiative transfer in heterogeneous 3-D vegetation canopies. *Remote*  
942 *Sensing of Environment*, *58*, 131 – 156.
- 943 Gerber, F., Marion, R., Oliosio, A., Jacquemoud, S., da Luz, B. R., & Fabre,  
944 S. (2011). Modeling directional–hemispherical reflectance and transmit-  
945 tance of fresh and dry leaves from 0.4  $\mu\text{m}$  to 5.7  $\mu\text{m}$  with the PROSPECT-  
946 VISIR model. *Remote Sensing of Environment*, *115*, 404–414.
- 947 Hale, G. M., & Querry, M. R. (1973). Optical constants of water in the  
948 200-nm to 200- $\mu\text{m}$  wavelength region. *Appl. Opt.*, *12*, 555–563.
- 949 Hochberg, E. J., Andrefouet, S., & Tyler, M. R. (2003). Sea surface correc-  
950 tion of high spatial resolution Ikonos images to improve bottom mapping



- 951 in near-shore environments. *Geoscience and Remote Sensing, IEEE Trans-*  
952 *actions on*, 41, 1724–1729.
- 953 Jacquemoud, S., Bacour, C., Poilv, H., & Frangi, J.-P. (2000). Comparison  
954 of four radiative transfer models to simulate plant canopies reflectance:  
955 Direct and inverse mode. *Remote Sensing of Environment*, 74, 471 – 481.
- 956 Jacquemoud, S., & Baret, F. (1990). PROSPECT: A model of leaf optical  
957 properties spectra. *Remote sensing of environment*, 34, 75–91.
- 958 Jacquemoud, S., Ustin, S., Verdebout, J., Schmuck, G., Andreoli, G., &  
959 Hosgood, B. (1996). Estimating leaf biochemistry using the PROSPECT  
960 leaf optical properties model. *Remote Sensing of Environment*, 56, 194 –  
961 202.
- 962 Jacquemoud, S., Verhoef, W., Baret, F., Bacour, C., Zarco-Tejada, P. J.,  
963 Asner, G. P., François, C., & Ustin, S. L. (2009). PROSPECT+SAIL  
964 models: A review of use for vegetation characterization. *Remote Sensing*  
965 *of Environment*, 113, S56 – S66.
- 966 Jay, S., Hadoux, X., Gorretta, N., & Rabatel, G. (2014). Potential of hy-  
967 perspectral imagery for nitrogen content retrieval in sugar beet leaves. In  
968 *Proc. Int. Conf. Ag. Eng., AgEng2014, Zurich*. The European Society of  
969 Agricultural Engineers (EurAgEng).
- 970 Jay, S., Rabatel, G., Hadoux, X., Moura, D., & Gorretta, N. (2015). In-field  
971 crop row phenotyping from 3D modeling performed using Structure from  
972 Motion. *Computers and Electronics in Agriculture*, 110, 70–77.

- 973 Ji-Yong, S., Xiao-Bo, Z., Jie-Wen, Z., Kai-Liang, W., Zheng-Wei, C., Xiao-  
974 Wei, H., De-Tao, Z., & Holmes, M. (2012). Nondestructive diagnostics of  
975 nitrogen deficiency by cucumber leaf chlorophyll distribution map based on  
976 near infrared hyperspectral imaging. *Scientia horticultrae*, *138*, 190–197.
- 977 Knyazikhin, Y., Schull, M. a., Stenberg, P., Möttus, M., Rautiainen, M.,  
978 Yang, Y., Marshak, A., Latorre Carmona, P., Kaufmann, R. K., Lewis,  
979 P., Disney, M. I., Vanderbilt, V., Davis, A. B., Baret, F., Jacquemoud, S.,  
980 Lyapustin, A., & Myneni, R. B. (2013). Hyperspectral remote sensing of  
981 foliar nitrogen content. *Proceedings of the National Academy of Sciences*,  
982 *110*, E185–E192.
- 983 Lati, R. N., Filin, S., & Eizenberg, H. (2013). Estimating plant growth  
984 parameters using an energy minimization-based stereovision model. *Com-  
985 puters and Electronics in Agriculture*, *98*, 260–271.
- 986 Mahlein, A.-K., Rumpf, T., Welke, P., Dehne, H.-W., Plümer, L., Steiner, U.,  
987 & Oerke, E.-C. (2013). Development of spectral indices for detecting and  
988 identifying plant diseases. *Remote Sensing of Environment*, *128*, 21–30.
- 989 Miesch, C., Briottet, X., & Kerr, Y. (2002). Bidirectional reflectance of a  
990 rough anisotropic surface. *International Journal of Remote Sensing*, *23*,  
991 3107–3114.
- 992 Moorthy, I., Miller, J. R., & Noland, T. L. (2008). Estimating chlorophyll  
993 concentration in conifer needles with hyperspectral data: An assessment  
994 at the needle and canopy level. *Remote Sensing of Environment*, *112*,  
995 2824–2838.

- 996 Nicodemus, F. E., Richmond, J. C., Hsia, J. J., Ginsberg, I. W., & Limperis,  
997 T. (1977). *Geometrical considerations and nomenclature for reflectance*  
998 volume 160. US Department of Commerce, National Bureau of Standards  
999 Washington, DC, USA.
- 1000 Nicotra, A., Hofmann, M., Siebke, K., & Ball, M. (2003). Spatial patterning  
1001 of pigmentation in evergreen leaves in response to freezing stress. *Plant,*  
1002 *Cell & Environment*, *26*, 1893–1904.
- 1003 Saltelli, A., Tarantola, S., & Chan, K.-S. (1999). A quantitative model-  
1004 independent method for global sensitivity analysis of model output. *Tech-*  
1005 *nometrics*, *41*, 39–56.
- 1006 Schaepman-Strub, G., Schaepman, M., Painter, T., Dangel, S., & Mar-  
1007 tonchik, J. (2006). Reflectance quantities in optical remote sensing - defi-  
1008 nitions and case studies. *Remote sensing of environment*, *103*, 27–42.
- 1009 Schlemmer, M., Gitelson, A., Schepers, J., Ferguson, R., Peng, Y., Shanahan,  
1010 J., & Rundquist, D. (2013). Remote estimation of nitrogen and chlorophyll  
1011 contents in maize at leaf and canopy levels. *International Journal of Ap-*  
1012 *plied Earth Observation and Geoinformation*, *25*, 47 – 54.
- 1013 Stuckens, J., Somers, B., Delalieux, S., Verstraeten, W., & Coppin, P. (2009).  
1014 The impact of common assumptions on canopy radiative transfer simula-  
1015 tions: A case study in citrus orchards. *Journal of Quantitative Spectroscopy*  
1016 *and Radiative Transfer*, *110*, 1–21.
- 1017 Ustin, S. L., Gitelson, A. A., Jacquemoud, S., Schaepman, M., Asner, G. P.,  
1018 Gamon, J. A., & Zarco-Tejada, P. (2009). Retrieval of foliar information

- 1019 about plant pigment systems from high resolution spectroscopy. *Remote*  
1020 *Sensing of Environment*, 113, S67–S77.
- 1021 Vanderbilt, V. C., & Grant, L. (1985). Plant canopy specular reflectance  
1022 model. *Geoscience and Remote Sensing, IEEE Transactions on*, (pp. 722–  
1023 730).
- 1024 Verhoef, W. (1984). Light scattering by leaf layers with application to canopy  
1025 reflectance modeling: The SAIL model. *Remote Sensing of Environment*,  
1026 16, 125 – 141.
- 1027 Verrelst, J., Camps-Valls, G., Muñoz-Marí, J., Rivera, J. P., Veroustraete,  
1028 F., Clevers, J. G., & Moreno, J. (2015). Optical remote sensing and the re-  
1029 trieval of terrestrial vegetation bio-geophysical properties—a review. *ISPRS*  
1030 *Journal of Photogrammetry and Remote Sensing*, in press, .
- 1031 Vigneau, N., Ecartot, M., Rabatel, G., & Roumet, P. (2011). Potential  
1032 of field hyperspectral imaging as a non destructive method to assess leaf  
1033 nitrogen content in wheat. *Field Crops Research*, 122, 25–31.
- 1034 Wallach, D., Makowski, D., Jones, J. W., & Brun, F. (2014). *Working*  
1035 *with dynamic crop models. Methods, tools and examples for agriculture*  
1036 *and environment*. Londres, GBR: Academic Press - Elsevier.
- 1037 Zarco-Tejada, P. J., Miller, J., Morales, A., Berjón, A., & Aguera, J. (2004).  
1038 Hyperspectral indices and model simulation for chlorophyll estimation in  
1039 open-canopy tree crops. *Remote Sensing of Environment*, 90, 463–476.
- 1040 Zarco-Tejada, P. J., Rueda, C., & Ustin, S. (2003). Water content estimation

1041 in vegetation with MODIS reflectance data and model inversion methods.  
1042 *Remote Sensing of Environment*, 85, 109–124.

1043 **List of Figures**

1044	1	Angle representation. . . . .	9
1045	2	Experimental setup for the horizontal (a) and tilted (b-c) con-	
1046		figurations. For the VNIR camera, the corresponding average	
1047		incident angles $\bar{\theta}_i$ are 20° (a), 40° (b) and 0° (c). For the SWIR	
1048		camera, the corresponding average incident angles $\bar{\theta}_i$ are 30°	
1049		(a), 10° (b) and 50° (c). . . . .	17
1050	3	First-order sensitivity indices and interactions for (a) PROSPECT	
1051		in the VNIR range, (b) PROSPECT in the SWIR range, (c)	
1052		PROCOSINE in the VNIR range, and (d) PROCOSINE in	
1053		the SWIR range ( $\theta_s = 26^\circ$ ). . . . .	26
1054	4	Fitting results obtained for the VNIR range (a-c) and the	
1055		SWIR range (d-f) using the pseudo-BRF model (b,e) and the	
1056		radiance model (c,f). Solid (resp. dashed) lines correspond to	
1057		measurements (resp. simulations). Blue curves correspond to	
1058		areas strongly affected by specular reflection, while red curves	
1059		correspond to areas characterized by a high incident angle. . .	30

1060	5	<p><math>C_{ab}</math> estimation results (mean +/- standard deviation) obtained with PROSPECT (blue), the pseudo-BRF based PROCOSINE model (orange), and the radiance-based PROCOSINE model (green) and with <math>\bar{\theta}_i = 20^\circ</math> (a-c), <math>\bar{\theta}_i = 0^\circ</math> (d-f) and <math>\bar{\theta}_i = 40^\circ</math> (g-i). The <math>R^2</math> and RMSE values are computed for actual <math>C_{ab}</math> values lower than <math>40 \mu\text{g}\cdot\text{cm}^{-2}</math> and are given in parentheses. . . . .</p>	31
1061			
1062			
1063			
1064			
1065			
1066			
1067	6	<p>Histograms of estimated <math>\theta_i</math> values for every pixel for the VNIR range and the three acquisition configurations (<math>\bar{\theta}_i = 0^\circ</math>, <math>\bar{\theta}_i = 20^\circ</math>, and <math>\bar{\theta}_i = 40^\circ</math>): (a) pseudo-BRF based PROCOSINE model, and (b) radiance-based PROCOSINE model. . . . .</p>	33
1068			
1069			
1070			
1071	7	<p><math>C_w</math> estimation results (mean +/- standard deviation) obtained with PROSPECT (blue), the pseudo-BRF based PROCOSINE model (orange), and the radiance-based PROCOSINE model (green) and with <math>\bar{\theta}_i = 30^\circ</math> (a-c), <math>\bar{\theta}_i = 10^\circ</math> (d-f) and <math>\bar{\theta}_i = 50^\circ</math> (g-i). <math>R^2</math> and RMSE values are given in parentheses. . . . .</p>	35
1072			
1073			
1074			
1075			
1076	8	<p><math>C_m</math> estimation results (mean +/- standard deviation) obtained with PROSPECT (blue), the pseudo-BRF based PROCOSINE model (orange), and the radiance-based PROCOSINE model (green) and with <math>\bar{\theta}_i = 30^\circ</math> (a-c), <math>\bar{\theta}_i = 10^\circ</math> (d-f) and <math>\bar{\theta}_i = 50^\circ</math> (g-i). <math>R^2</math> and RMSE values are given in parentheses. . . . .</p>	36
1077			
1078			
1079			
1080			
1081	9	<p>Histograms of estimated <math>\theta_i</math> values in every pixel for the SWIR range and the three acquisition configurations (<math>\bar{\theta}_i = 10^\circ</math>, <math>\bar{\theta}_i = 30^\circ</math>, and <math>\bar{\theta}_i = 50^\circ</math>): (a) pseudo-BRF based PROCOSINE model, and (b) radiance-based PROCOSINE model. . . . .</p>	37
1082			
1083			
1084			

1085	10	Estimated maps obtained using PROSPECT in the VNIR (a-	
1086		c) and SWIR (d-f) ranges: (a) true color composite image,	
1087		(b) $C_{ab}$ , (c) $C_{bp}$ , (d) false color composite image (using bands	
1088		1458 nm, 2202 nm and 1662 nm), (e) $C_w$ , (f) $C_m$ . . . . .	44
1089	11	Estimated maps obtained using the radiance-based PROCOSINE	
1090		model in the VNIR (a-e) and SWIR (f-j) ranges: (a)	
1091		true color composite image, (b) $C_{ab}$ , (c) $C_{bp}$ , (d) $b_{spec}$ , (e) $\theta_i$ ,	
1092		(f) false color composite image (using bands 1458 nm, 2202 nm	
1093		and 1662 nm), (g) $C_w$ , (h) $C_m$ , (i) $b_{spec}$ , (j) $\theta_i$ . . . . .	45
1094	12	Estimated maps obtained in the SWIR range using the radiance-	
1095		based PROCOSINE model (b-f) and PROSPECT (g-i): (a)	
1096		false color composite image (using bands 1458 nm, 2202 nm	
1097		and 1662 nm), (b) $b_{spec}$ , (c) $\theta_i$ , (d) $N$ , (e) $C_w$ , (f) $C_m$ , (g) $N$ ,	
1098		(h) $C_w$ , (i) $C_m$ . . . . .	47
1099	13	Use of the PROCOSINE model for image pretreatment in	
1100		the VNIR (a-c) range: (a) DHR image reconstructed with	
1101		PROSPECT and estimated parameters, (b) <i>SBRI</i> map (Mahlein	
1102		et al., 2013) obtained with the original image, and (c) <i>SBRI</i>	
1103		map (Mahlein et al., 2013) obtained with the reconstructed	
1104		image. . . . .	49